Front. Phys. 13(6), 132112 (2018)
https://doi.org/10.1007/s11467-018-0844-5

REVIEW ARTICLE

# Precision mass measurements of short-lived nuclides at HIRFL-CSR in Lanzhou

**Ming-Ze Sun**[1,2], **Xiao-Hong Zhou**[1,†], **Meng Wang**[1,‡], **Yu-Hu Zhang**[1], **Yu. A. Litvinov**[1,3]

[1] *Key Laboratory of High Precision Nuclear Spectroscopy and Center for Nuclear Matter Science, Institute of Modern Physics, Chinese Academy of Sciences, Lanzhou 730000, China*
[2] *University of Chinese Academy of Sciences, Beijing 100049, China*
[3] *GSI Helmholtzzentrum für Schwerionenforschung, Planckstraße 1, 64291 Darmstadt, Germany*
*Corresponding authors. E-mail:* [†] *zxh@impcas.ac.cn,* [‡] *wangm@impcas.ac.cn*
*Received July 15, 2018; accepted August 2, 2018*

In recent years, extensive short-lived nuclear mass measurements have been carried out at the Heavy-Ion Research Facility (HIRFL) in Lanzhou using Isochronous Mass Spectrometry (IMS). The obtained mass values have been successfully applied to nuclear structure and astrophysics studies. In this contribution, we give a brief introduction to the nuclear mass measurements at HIRFL-CSR facility. Main technical developments are described and recent results are summarized. Furthermore, we envision the future perspective for the next-generation storage ring facility HIAF in Huizhou.

**Keywords** nuclear mass, short-lived nuclei, storage ring, isochronous mass spectrometry

**PACS numbers** 03.65.Yz, 02.70.-c, 05.30.-d, 05.10.Gg

Contents



*Special Topic: Simplicity, Symmetry, and Beauty of Atomic Nuclei (Eds. Jie Meng, Takaharu Otsuka & Yu-Min Zhao).

## 1 Introduction

The history of nuclear mass measurements is almost as old as that of nuclear physics itself [1], and the mass spectrometry has made great contributions to the understanding of nuclear structure, nuclear astrophysics, as well as testing of the standard model and fundamental symmetries [2, 3]. In the early experiments, Thomson built the first mass spectrograph [4] and discovered the isotopic nature of the chemical elements. Later, his student Aston developed new instruments to improve the resolving power, and from his precise measurements he found out the "mass defect" of atomic nuclei [5, 6]. These pioneering experimental results led to the development of the first successful theoretical descriptions of the nucleus,



Frontiers of Physics

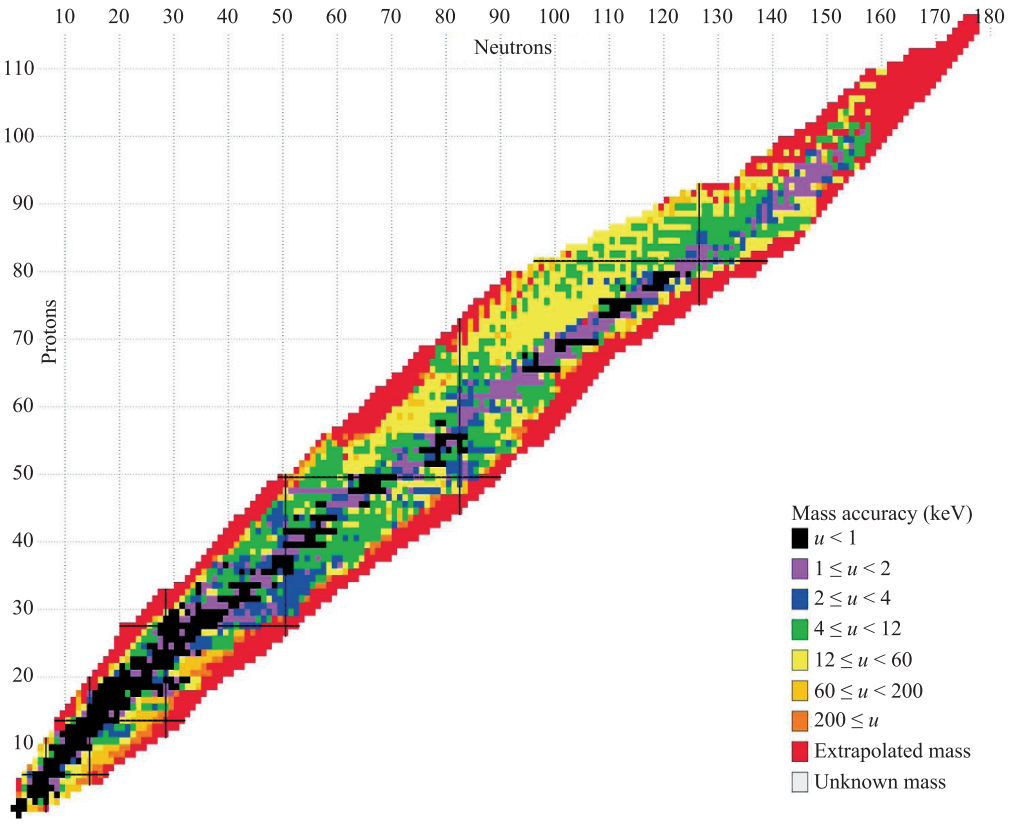


**Fig. 1** The nuclear chart with experimentally known masses in AME′16, where the mass accuracies of the nuclei are presented. Reproduced from Ref. [20].

i.e., the liquid drop model [7–9], and boosted the interest to atomic mass measurements. Afterwards, the development of high precision mass spectrometers by Dempster [10], Mattauch [11], and Ewald [12] contributed to the first mass tables of stable isotopes with their mass values based on $^{12}$C [13].

Over the decades, more and more mass-spectrometry methods were invented and refined [14]. The advent and application of radioactive ion beam facilities [15] and novel mass spectrometers [14] have strikingly enlarged the number of known isotopes [16, 17]. Today, from 7000 to 9000 nuclides are predicted to be found in nature [18, 19] while 2479 of their masses have been measured experimentally and compiled in the latest Atomic Mass Evaluation (AME'16) [20]. Figure 1 shows the known mass region of the nuclear chart [20]. As can be seen, the nuclides with still unknown or low-accuracy masses are mostly exotic nuclei which lie far from the valley of $\beta$-stability. These nuclides might have new properties which are different from the stable ones and are of great importance for the understanding of the nuclear structure at the outskirts of the nuclear chart. For example, the nuclear shell structure tends to change towards the driplines. New magic numbers in neutron-rich mass region have been theoretically predicted [21–23] and several new magic numbers have been observed in experiments [24–27]. Furthermore, the mass values of the exotic nuclei are important parameters for the investigation of the explosive nucleosynthesis processes in stellar environments, as discussed in Refs. [28–30]. Nevertheless, the precision mass measurements of these exotic nuclei are great experimental challenges due to their short lifetimes and tiny production cross-sections in nuclear reactions. Additionally, they can only be investigated if they are efficiently separated from the non-reacted primary beam and all abundant contaminants [31]. Therefore, experimentalists try to conquer these challenges by developing new techniques [14].

Nowadays, frequency and revolution time measurements in ion traps and storage rings provide the highest mass accuracy and resolving power. For the latter, the storage-ring mass spectrometry, has become one of the most efficient and fast experimental techniques for direct nuclear mass measurements [32–36]. There are presently three storage ring facilities used worldwide, which are ESR at GSI in Darmstadt/Germany, the R3 storage ring

at RIKEN in Saitama/Japan, and the CSRe at IMP in Lanzhou/China. In this article, we give a brief introduction to the HIRFL-CSR facility and its experimental techniques. Recent results are summarized and their impact on nuclear physics and astrophysics are discussed. In addition, we outline the technical developments and the envisioned future perspectives for the next-generation storage ring facility HIAF (High Intensity heavy ion Accelerator Facility) which will be built in Huizhou.

## 2 Experimental details

### 2.1 Principle of IMS at storage rings

Heavy-ion storage rings are complicated facilities which consist of various components, such as kicker magnets to inject and extract particles, dipole magnets to bend the trajectories, quadrupole magnets to focus the particles, sextupole magnets to correct for aberrations, cooling devices, de-/acceleration cavities, and diagnostic setups [37]. For each ion circulating in a storage ring, the revolution time $T$ is related with its mass-to-charge $m/q$ ratio via the following expression:

$$T = \frac{L}{c} \cdot \sqrt{1 + \left(\frac{mc}{q}\right)^2 \cdot \frac{1}{(B\rho)^2}}, \tag{1}$$

where $L$ and $B\rho$ are the orbital length and magnetic rigidity of the ion, respectively, and $c$ is the speed of light. The relationship between $L$ and $B\rho$ can be described by the momentum compaction factor $\alpha_p$:

$$\alpha_p \equiv \frac{\mathrm{d}L/L}{\mathrm{d}(B\rho)/(B\rho)}. \tag{2}$$

Therefore, we can deduce that the ions with a same magnetic rigidity $B\rho$ share a same orbital length $L$ despite their different ion species. Thus, it is easy to determine the $m/q$ of the ion via the measured revolution time $T$.

However, within a magnetic rigidity acceptance $\Delta B\rho$ of the storage ring, the velocity spread of the ions will induce spread in orbital lengths. The fractional revolution time change $\Delta T/T$ is determined in the first order approximation by

$$\frac{\Delta T}{T} = \frac{1}{\gamma_t^2} \cdot \frac{\Delta(m/q)}{(m/q)} - \left(1 - \frac{\gamma^2}{\gamma_t^2}\right) \cdot \frac{\Delta v}{v}, \tag{3}$$

where $v$ is the velocity of the ion and $\gamma = [1-(v/c)^2]^{-1/2}$ is the relativistic Lorentz factor. $\gamma_t$ is the so-called "transition energy", defined as [38]

$$\gamma_t \equiv \frac{1}{\sqrt{\alpha_p}}. \tag{4}$$

By inspecting Eq. (3) one can see that the revolution times of the ions directly reflect $m/q$ ratios of the stored ions if the second term on the right-hand side, which contain their velocity spread, can be eliminated. One way to achieve this goal is to use a special ion-optical setting of the ring and inject the ions of interest with $\gamma = \gamma_t$. This is the principle of the Isochronous Mass Spectrometry (IMS). In this particular operation mode, the velocity spread of the ion is compensated by the length of the closed orbit inside the ring. In this way, the revolution times are a direct measure of $m/q$ of the ions, independent of their velocity spread $\Delta v/v$. Owing to the large acceptance of the ring and no requirement for beam cooling, the IMS is an ideal tool for the mass measurement of short-lived nuclides with tiny production cross sections.

### 2.2 Experimental facility

The HIRFL-CSR facility has been put into operation since 2007 at the Institute of Modern Physics, Chinese Academy of Sciences [39, 40]. As illustrated in Fig. 2(a), its high-energy part consists of the heavy-ion synchrotron CSRm, the in-flight fragment separator RIBLL2, and the experimental cooler-storage ring CSRe. Heavy-ion beams are accelerated in CSRm to a relativistic energy of 350-480 MeV/u. Then the high-energy beams are fast extracted and focused upon a 10-15 mm beryllium target placed at the entrance of RIBLL2. The reaction fragments are separated in flight with the RIBLL2 and a cocktail beam is injected into the CSRe. Within the $B\rho$ acceptance of CSRe around ±0.2%, the selected ions are transmitted and stored. The CSRe is tuned in an isochronous ion-optical mode with the transition energy

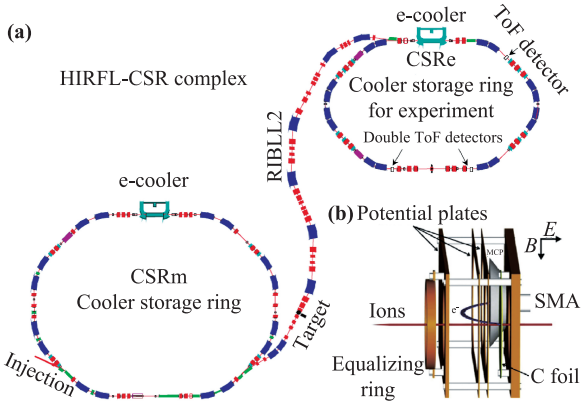


**Fig. 2** **(a)** Schematic layout of the high-energy part of HIRFL-CSR facility, which consists of the heavy-ion synchrotron CSRm, the in-flight fragment separator RIBLL2, and the experimental cooler-storage ring CSRe. **(b)** Schematic view of the time-of-flight (ToF) detector.

$\gamma_t$ determined. The energy of the primary beam is chosen so that the $\gamma$ of the ion species of interest after the production target approximates to the $\gamma_t$.

The revolution time of the stored ions are measured by a dedicated time-of-flight (ToF) detector [41], whose schematic view is shown in Fig. 2(b). The detector is equipped with a 19 μg/cm$^2$ thin carbon foil of 40 mm in diameter and a micro channel plate (MCP) counter. At each passage of the stored ions, secondary electrons are released from the foil surface and guided isochronously by perpendicularly arranged electric (E) and magnetic (B) fields to the MCP counter. The signals from the MCP are directly collected by a fast oscilloscope Tektronix DPO 71254 at a sampling rate of 50 GHz. The recording time is typically 200 μs for each injection, which corresponds to approximately 300 revolutions. Figure 3 shows a part of a typical recorded signal sequence of a few stored ions. The time resolution of the ToF detector is about 50 ps, and the detection efficiency varies from 20% to 70% depending on the charge and the overall number of stored ions [41]. More details of the detector can be found in Ref. [41].

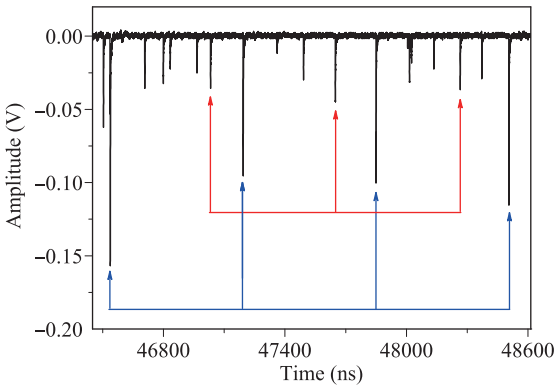


**Fig. 3** Signals from the ToF detector are recorded by a fast oscilloscope. Pulse signals are produced when the stored ions pass through the carbon foil. The blue and red arrows represent the periodic signals produced by two ions at every revolution, respectively.

### 2.3 Data analysis

The recorded periodic timing signals are used to determine the revolution time of each individual ion. Taking the $^{58}$Ni experiment for example, the deduced revolution time spectrum is presented in Fig. 4 [42]. The revolution time peaks are identified by comparing with the simulated ones [43–45]. To determine the masses of the target nuclei, the nuclei with experimentally known masses are used to fit $m/q$ versus $T$ by employing a polynomial function. The lowest possible order is applied to fit the data so as to avoid overfitting. Thus, a third-order polynomial function is chosen in our data analysis. Up to now, no significant systematic errors are observed in our mass measurements at CSRe, and a relative uncertainty of $10^{-6}$–$10^{-7}$ has been achieved, depending on the statistics of the specific nuclei and the distance of its $\gamma$ value to the $\gamma_t$ set in experiments.

## 3 Technical developments

### 3.1 Time correction of magnetic field

As we know, the performance of mass spectrometries are deeply affected by the instabilities of facilities. At HIRFL-CSR, the instabilities of the magnetic fields of CSRe may cause small shifts in the entire revolution

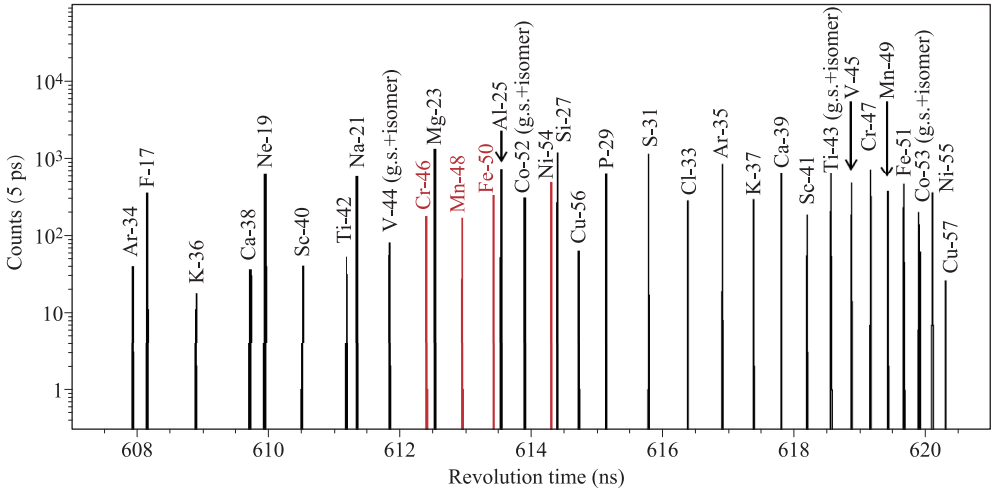


**Fig. 4** Part of the revolution time spectrum of $^{58}$Ni projectile fragments zoomed in the time window of 607 ns $\leq T \leq$ 621 ns. The red peaks indicate those nuclei of interest. Reproduced from Ref. [42].

time spectrum at different injections, which reduces the achievable precision of the measured mass values. Since the IMS experiments were pioneered at GSI, several conventional methods have been developed to correct the magnetic drift [46, 47]. However, the expected resolving power were not achieved at CSRe when applying the same correction methods due to the less stable magnetic field (typically $\frac{\delta B}{B} \approx 10^{-5}$–$10^{-4}$) and lower statistics. To overcome this problem, a series of methods are being developed at CSRe to correct the magnetic drifts in IMS experiments.

Assuming the magnetic fields of CSRe are stable within the measurement time (200 μs) of individual injections, the absolute revolution time of each nuclide changes correspondingly when the magnetic fields change for different injections. However, their relative revolution times of different ion species in each injection do almost not change. Therefore, the relative revolution times can be employed instead of the absolute values, which are the time differences of the revolution time of a selected reference nuclide to that of all other ion species in a given injection. The revolution times in each individual injection are shifted according to the relative revolution times and the independent revolution time spectra are formed by combining the injections with the same kind of reference together. Figure 5 presents the uncorrected revolution time spectrum (a), the corrected spectrum using the conventional method (b) [47] and the corrected spectrum using this method (c) [44] for $^{53}Co^{27+}$ ion. It can be seen that the 3174.3 keV isomer of $^{53}$Co is well separated from the ground state by using this method. The disadvantage of this method is that the increase of the revolution time spreads due to the artificial setting of the spread for the reference ion as zero. Furthermore, the measurements require the reference nuclide to be presented in a given injection, and consequently the injections without the reference nuclide are lost. Therefore, the nuclides with high statistics and much small standard deviations of revolution times are selected as reference nuclides.

For the experiments in which no suitable reference nuclides presented, a gain-matched method is employed [50, 51]. This method was inspired by the method of $\gamma$ spectroscopy. Although the magnetic fields of CSRe dipole magnets can not be recorded in the timescale of 200 μs, they are continuously monitored and used to identify time intervals of relatively constant magnetic fields. Therefore, the entire data could be grouped according to these time intervals, and the sub-spectra are obtained. One of them is chosen as the standard spectrum. Each sub-spectrum has a relative shift of revolution time compared to the standard spectrum. Taking the relative shifts into account, all sub-spectra are combined into a common revolution time spectrum. The disadvantage of this method is that the magnetic field instabilities during the time intervals of the sub-spectra are not considered.

As the instabilities of magnetic fields slowly vary between individual injections, a new method called weighted shift was developed to accurately deduce the revolution times of the stored ions and their standard deviations. The mean values and the standard deviations, including the contribution due to unstable magnetic fields, of the measured revolution times are connected via a set of equations, and the set of equations is solved iteratively in mathematics. The mean revolution times and the standard deviations without the latter contribution are calculated, which are then used for the mass determination in a standard way. The details of the method can be found in Ref. [52]. The comparison of the standard deviations of revolution time distributions obtained with weighted shift method (red and green squares) and gain-matched method (black circles) is shown in Fig. 6. It can be seen that smaller standard deviations of revolution time distributions were achieved with the weighted shift method. By using this method, all the identified nuclides are selected as the reference nuclides so that almost all the obtained data can be used in

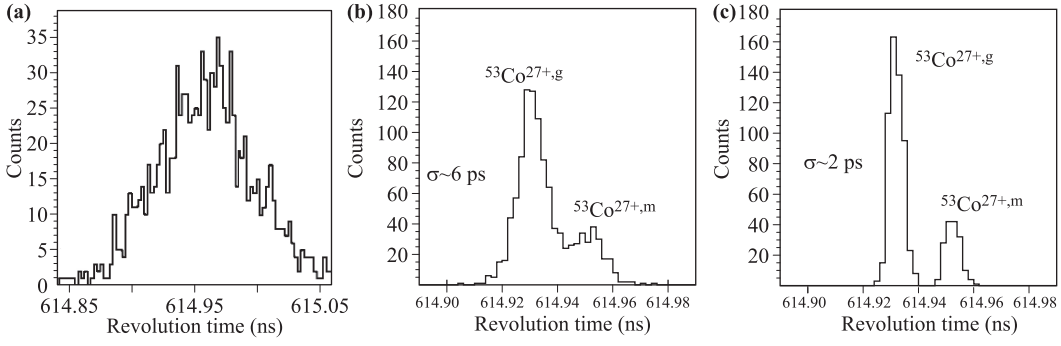


**Fig. 5** **(a)** The revolution time spectra of ground and isomeric states of $^{53}$Co obtained with uncorrected absolute values and **(b)** the conventional method of Ref. [47] and **(c)** the newly developed method [44]. Note that the deduced excitation energy of the isomer is in excellent agreement with the literature value [48]. Reproduced from Refs. [44, 49].

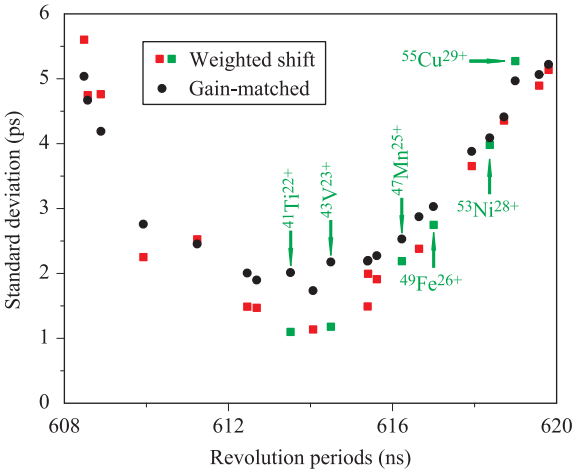


**Fig. 6** The comparison of the standard deviations obtained with weighted shift method (red and green squares) and gain-matched method in Refs. [50, 51] (black circles). A range of revolution times of 608 ns $\leq T \leq$ 620 ns is considered. Reproduced from Ref. [52].

the analysis. Due to these advantages over other methods, this method has been applied to the data analysis of recent experiments [27, 42, 53–55].

### 3.2 The transition energy $\gamma_t$ measurement

As mentioned above, the IMS is based on the isochronous setting of the storage ring. One of the major parameters in this setting is the transition energy $\gamma_t$, which reflects the ratio between the relative change in the orbital length and the relative change in the magnetic rigidity of the stored ions [34]. It has been a challenge to determine the value of $\gamma_t$, especially to monitor its variation during IMS experiments. A new method has been developed to measure the $\gamma_t$ online during IMS experiments by using the acquired experimental data [56].

The recorded signals are used to determine the revolution time of the stored ion. The periodic signals from each individual ion are fitted by a second order polynomial function with fit coefficients $a_0$, $a_1$, and $a_2$ as follows:

$$t = a_0 + a_1 \cdot turn + a_2 \cdot turn^2. \tag{5}$$

The expression for coefficient $a_2$ can be deduced [56]:

$$a_2 = -\frac{1}{2} \cdot \left(\frac{1}{\gamma^2} - \frac{1}{\gamma_t^2}\right) \cdot \frac{\gamma}{\gamma+1} \cdot \frac{\delta E_k}{E_k} \cdot T, \tag{6}$$

where $E_k$ and $\delta E_k$ are the kinetic energy and the average energy loss in the foil. The details of the deduction can be found in Ref. [56].

According to Eq. (6), the coefficient $a_2$ is determined by the parameters of the ion $\gamma$, $\delta E_k$, $E_k$, $T$, and $\gamma_t$. $\delta E_k$ is related to the thickness of the carbon foil. Thus, once the ion is identified the fitting coefficient $a_2$ can be calculated. Figure 7 shows the relationship between the average revolution time of each nuclide and its corresponding average coefficient $a_2$ [56]. The open rectangles represent the experimental data obtained in $^{58}$Ni experiment [53] while the red filled circles represent the results calculated by using Eq. (6) assuming $\gamma_t = 1.3971$ and the carbon foil thickness of $d = 21.6$ μg/cm$^2$. It can be seen that the calculations agree well with the experimental data. The experimental data is very sensitive to the assumed thickness of the foil $d$ and the $\gamma_t$, and thus the two parameters can be calculated in this way.

The carbon foil thickness $d$ and the $\gamma_t$ are measured in one-hour step in $^{58}$Ni experiment [53]. As shown in Fig. 8(a), two adjustments to the CSRe were performed during 24 hours while the 3 time periods are label with "setting 1–3", respectively. At the time mark of 11:00, the quadrupoles of CSRe were adjusted, causing the change of the $\gamma_t$ from 1.396 to 1.402. Then at about 18:30 time mark, a mechanical slit was installed in the CSRe

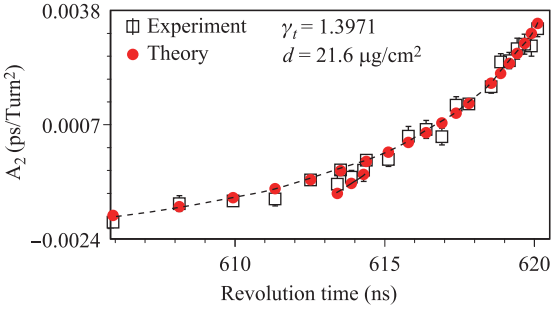


**Fig. 7** The relationship between average revolution time of each nuclide and its corresponding average fitting coefficient $a_2$. The open rectangles represent the experimental data obtained in $^{58}$Ni experiment while the red filled circles represent results calculated by using Eq. (6) assuming $\gamma_t = 1.3971$ and the thickness of carbon foil $d = 21.6$ μg/cm$^2$. Reproduced from Ref. [56].

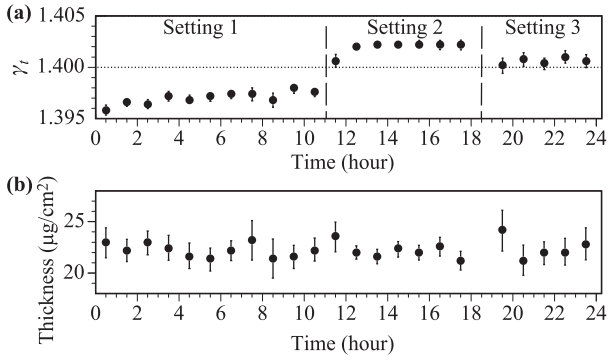


**Fig. 8** **(a)** The dependence of $\gamma_t$ and **(b)** the thickness of carbon foil $d$ as a function of time. Reproduced from Ref. [56].

aperture, leading to a reduction in the ring acceptance and a change of the $\gamma_t$ from 1.402 to 1.400. The latter adjustment indicates that the $\gamma_t$ is not constant over the ring acceptance. Although the $\gamma_t$ changes in different settings, the determined foil thickness keeps unchanged within uncertainties. To verify the measurement of $\gamma_t$, the characterisation of isochronous settings are identified from the plot of the standard deviations $\sigma_t$ of revolution time distributions. As illustrated in Fig. 9, the data for setting 1–3 are presented. The best isochronous ions are found at 614.808 ns, 612.977 ns, and 613.889 ns, respectively. By taking the length of the CSRe central orbital (128.801 m) into account, the corresponding $\gamma_t$ values can be roughly estimated to be 1.396, 1.402, and 1.400, in good agreement with the measured ones.

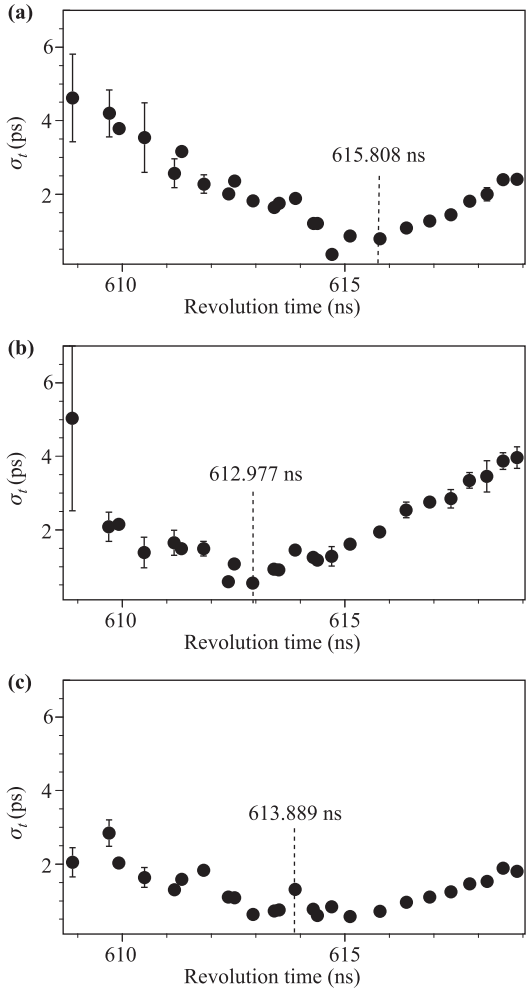


**Fig. 9** Standard deviations $\sigma_t$ of revolution time distributions as a function of the mean revolution times for different nuclides. Panels **(a)**, **(b)**, and **(c)** show the data for settings 1, 2 and 3 (see Fig. 8), respectively. The dashed lines indicated the corresponding isochronous settings. Reproduced from Ref. [56].

The measurement of $\gamma_t$ has been successfully applied as an online monitor of $\gamma_t$ during IMS experiments, as well as in providing information for particle selection on orbital length in IMS experiments with double ToF detectors. Furthermore, this method may be helpful for the measurements of the thicknesses of ultra-thin solid foils or internal targets or even rest-gas pressure [56].

### 3.3 IMS experiments with two time-of-flight detectors

The IMS in storage rings has been proven to be a powerful tool in mass measurement of exotic nuclei with half-lives down to several tens of microseconds. However, the inevitable velocity spread of the reaction products limit the mass resolution of the IMS [57, 58]. The method to correct the velocity spread of the stored ions by employing the velocity information has proven to be an effective way to improve the resolving power of IMS in simulations [57, 58]. For this purpose, two time-of-flight (double ToFs) detectors were installed in the straight section of CSRe [59, 60]. The schematic layout of the two detectors are shown in Fig. 10. More details of the detectors can be found in Refs. [59, 60].

Generally speaking, the velocity of an ion $v$ can be directly measured by the double ToF detectors:

$$v = \frac{s}{t_{down} - t_{up} - \Delta t}, \tag{7}$$

where $s$ is the path length of ions that fly over the two ToF detectors, and $t_{down}$ and $t_{up}$ are the timing point recorded by the two ToF detectors respectively. $\Delta t$ is the signal transmission time difference between the two ToF detectors. Figure 11 shows the relative uncertainty of the velocity of $^{32}Cl^{17+}$ measured, which is around $10^{-4}$.

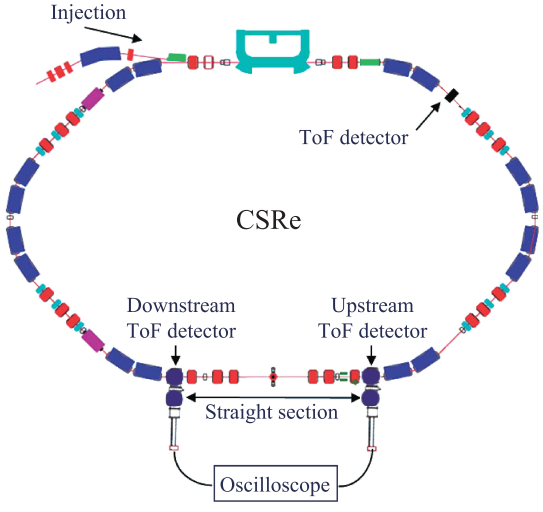


**Fig. 10** Schematic layout of the double ToF detectors at CSRe. An oscilloscope is employed to record the timing signals from the two detectors.

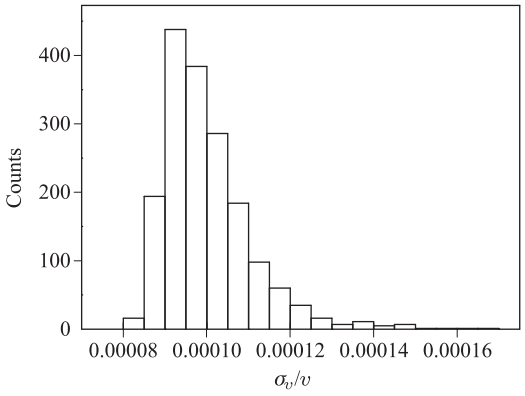


**Fig. 11** The relative uncertainty of the velocity of $^{32}Cl^{17+}$.

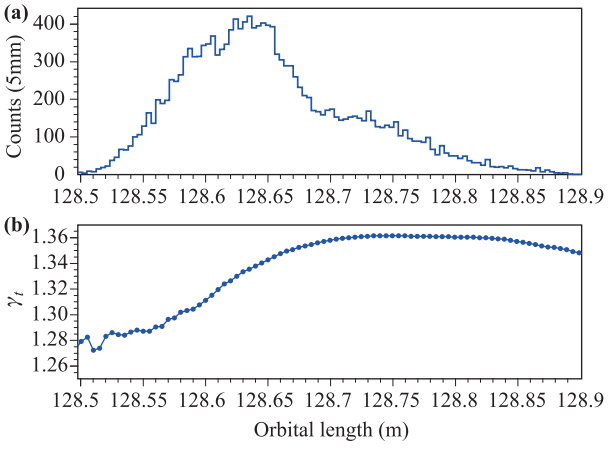


**Fig. 12** **(a)** The distribution of orbital length $L$. **(b)** $\gamma_t$ as a function of orbital length $L$.

With the velocity of each stored ion measured, the orbital length $L$ can be calculated by

$$L = v \cdot T. \tag{8}$$

Thus, the dependence of $\gamma_t$ on the orbital length $L$ can be evaluated by employing the method in the former subsection 3.2. Figure 12(a) shows the distribution of orbital length $L$ in an IMS experiment with double ToF detectors while the dependence of $\gamma_t$ on orbital length $L$ is represented in Fig. 12(b). It can be seen that the $\gamma_t$ nearly stays constant in the middle part while it changes rapidly for lower orbit lengths.

Before correcting the velocity spread, the ions are selected on the orbital length from 128.730 m to 128.830 m in order to ensure a nearly constant $\gamma_t$ value. The revolution time $T$ can be converted to the revolution time $T_0$ corrsponding to the reference orbit $L_0$ by [57]

$$T_0 = T + \left(1 - \frac{\gamma_t^2}{\gamma^2}\right) \cdot \frac{L_0 - L}{L} \cdot T. \tag{9}$$

To avoid extrapolation $L_0$ is defined as the central orbit 128.801 m. Figure 13 represents the preliminary results of the standard deviations of revolution time distributions by using the velocity information from double ToF detectors (red circle) compared to the results from single ToF detector (blue triangle). It can be seen that a higher resolving power for the entire revolution time spectrum has been achieved. This new IMS with double ToF detectors will allow us to improve the mass resolving power over the entire revolution time spectrum and give access to the mass measurement of a larger number of exotic nuclei.

### 3.4 Half-life measurement of fully stripped $^{94m}$Ru

Highly charged ions (HCI) are well-defined quantum systems whose decay modes and rates might be significantly different from those in neutral atoms [61–65]. The investigations of the bound-state $\beta$ decay [62, 65, 66] and orbital electron-capture decay in hydrogen-like and helium-like ions [67–69] have led to a deeper understanding in the nuclear decay mechanisms, as well as in the nucleosynthesis processes in astrophysics [70]. However, the measurement of short-lived isomeric decays in highly charged states is still difficult to approach due to lack of feasible measuring methods.

At HIRFL-CSR, the decay of the $8^+$ isomer in fully stripped ions $^{94}Ru^{44+}$ is observed during its circulation in the storage ring [71]. The $^{94}Ru^{44+}$ ions were produced via $^{112}Sn^{35+}$ projectile fragmentation and stored in the CSRe which is tuned into the isochronous ion-optical mode, optimized for the transmission of $^{94}Ru^{44+}$ ions. The revolution times are determined by using the

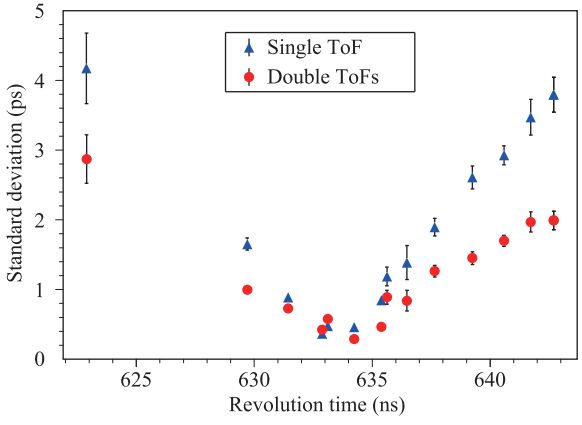


**Fig. 13** Preliminary results of the standard deviations of revolution time distributions using the velocity information from double ToF detectors (red circle) compared to the results from single ToF detector (blue triangle). It can be seen that a higher resolving power for the entire revolution time spectrum has been achieved.

recorded periodic timing signals. After particle identification and the correction of the magnetic field instabilities, a part of the revolution time spectrum zoomed in a narrow time window from 669.0 ns to 676.5 ns is illustrated in Fig. 14 [71], where the inset shows the well-separated two states of $^{94}$Ru$^{44+}$. By using the nuclides with accurately known masses as calibrants, the mass excesses of the isomeric and ground state of $^{94}$Ru were determined to be −79905(132) keV and −82531(72) keV respectively [71], in good agreement with the values of −79940(3) keV and −82584(3) keV from AME'16 [20].

It was impossible to identify the decay event simply by comparing the revolution times of the adjacent turns. This is because the revolution time difference between the isomeric and ground state of $^{94}$Ru$^{44+}$ ($\sim$ 11.9 ps) is much smaller than the intrinsic time resolution ($\sim$ 50 ps) of the timing detector [41] and the fluctuations caused by the finite emittance of the ion ($>$ 100 ps) [72]. Thus, a new method is developed. During the circulation in the storage ring, the change of revolution times of $^{94g,m}$Ru$^{44+}$ can be ignored despite the tiny energy loss when the ion passes through the carbon foil. In search of decay events, the passing times as a function of revolution turns of $^{94g,m}$Ru$^{44+}$ are fitted by a linear function in every consecutive 20-μs period. The revolution time of the corresponding time period can be extracted from the slope of the linear function. Thus, the dependence of revolution time on revolution turn is obtained. Two examples of no-decay and decay events are shown in Figs. 15(a) and (b) respectively. It can be seen that the revolution time is approximately constant in Fig. 15(a) while a sudden drop is observed in Fig. 15(b), which indicates the isomeric decay. The difference of the revolution times before and after the sudden drop is estimated

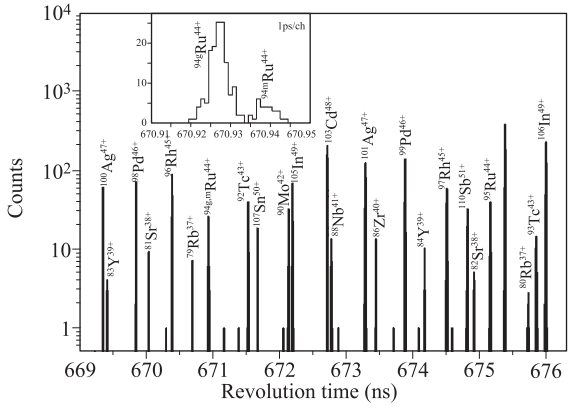


**Fig. 14** The revolution time spectrum zoomed in a narrow time window from 669.0 ns to 676.5 ns. The inset displays the well-resolved peaks of the ground (g) and isomeric (m) states of $^{94}$Ru$^{44+}$. Reproduced from Ref. [71].

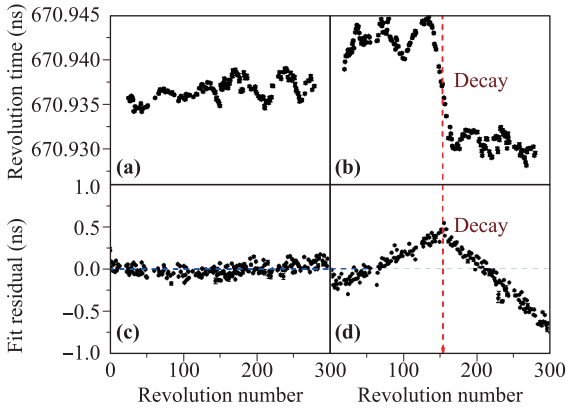


**Fig. 15** The revolution time as a function of revolution turn for no-decay **(a)** and decay **(b)** events. A sudden drop is observed in panel (b), indicating the isomeric decay. The residuals of the linear fit in whole circulating period for the two events are shown in panels **(c)** and **(d)**. The vertical lines in panels (b) and (d) indicate the decay time. Reproduced from Ref. [71].

to be 12 ps, corresponding to the excitation energy of the isomer. For further confirmation of the decay events, another linear function was employed to fit the passing times as a function of revolution turns in whole circulating period. Figures 15(c) and (d) represent the residual plot of the fitting. For the no-decay event, there is no evident structure in Fig. 15(c) because the $^{94}$Ru$^{44+}$ ion lies within the isochronous window. In Fig. 15(d), a clear kink is found in accordance with the sudden change of the revolution time in Fig. 15(b), demonstrating the decay of the isomer. To extract the decay time, the data of each decay events were divided into two parts by the turning point in the residual plot. In each part, a linear function is used to fit the passing times as a function of revolution turns. The intersection of the two fitting curves can be thus determined as the decay time, as shown in the vertical line in Figs. 15(b) and (d).

The isomeric half-life of $^{94m}$Ru$^{44+}$ was deduced to be 102(17) μs using the method in Ref. [73], in good agreement with the theoretical prediction 95(5) μs. This work proved the feasibility to study the decays of highly charged ions with half-lives down to several tens of microsecond using IMS. It is worth noting that $^{94m}$Ru$^{44+}$ is the shortest-lived nuclear state whose mass has ever been measured directly, and it is the first time for the measurement of mass and half-life simultaneously in the isochronous mode of the storage ring.

## 4 Recent results

Overall more than 60 mass values were measured with IMS at CSRe, and the masses of more than 20 nuclides

were determined for the first time in experiments. These experiments were performed with $^{78}$Kr [74], $^{86}$Kr [27], $^{36}$Ar, $^{58}$Ni [42, 50, 51, 53, 75], and $^{112}$Sn [54] primary beams. The nuclides with newly measured masses are illustrated in Fig. 16. Typical relative mass uncertainties of $\delta m/m = 10^{-6}$–$10^{-7}$ are achieved. Part of the data using $^{36}$Ar, $^{58}$Ni and $^{112}$Sn primary beams are still under analysis. The other mass values were included into AME′16 [20]. In the following, we present some recent results and their implications in nuclear structure and astrophysics, including $\beta$-decay properties of $^{52}$Ni, isospin symmetry in *sd*-shell nuclei, new magic number of $N = 32$ and Zr-Nb cycle in the *rp*-process. As the relative mass uncertainties of better than $1 \times 10^{-7}$ are reached for the first time with IMS at CSRe [42], the weak interaction studies about test of CVC hypothesis are also introduced.

### 4.1 Test of the isobaric multiplet mass equation in *pf*-shell nuclei and $\beta$-decay properties of $^{52}$Ni

The concept of isospin was introduced by Heisenberg and developed by Wigner [76]. As a nucleus consists of $Z$ protons and $N$ neutrons, the isospin projection is $T_z = (N - Z)/2$ with different total isospins $T \geq |T_z|$ for all states. It means that states in different isobaric nuclei with $T_z = T, T-1, \ldots, -T$ can have the same $T$. These states with same $J^\pi$ are called the isobaric analog states (IAS). Under the assumptions of only two-body charge-dependent effects, Wigner [77] and Weinberg [78] using first-order perturbation theory introduced the following quadratic equation to describe the mass excesses of IAS:

$$ME(\alpha, T, T_z) = a(\alpha, T) + b(\alpha, T)T_z + c(\alpha, T)T_z^2, \quad (10)$$

where $ME$ is the mass excess of a multiplet member, $a$, $b$, $c$ are parameters depending on $\alpha(A, J^\pi, \ldots)$. This local mass relation is called the isobaric multiplet mass equation (IMME). Usually a breakdown of IMME indicates that the effects of higher-order perturbation, many-body forces isospin mixing of the IAS with nearby states of same $J^\pi$ or inaccurate mass values should be considered [79]. In this situation, an extra term $dT_z^3$ and/or $eT_z^4$ is required, and $|d|/\sigma > 3$ is usually regarded as the breakdown of the quadratic form of the IMME.

To test the validity of quadratic form of IMME, the masses of four members of IASs are required in the isobaric quartets and quintets at least. For the *sd*-shell nuclei, the $d$ coefficients are compatible with zero within $3\sigma$, except for the $A = 32$ quintet and $A = 35$ quartet [80]. Furthermore, the breakdown of $A = 21, 31$ quartets were also found through recent precise mass measurements of $^{21}$Mg and $^{31}$Cl by penning traps [81, 82].

For the *pf*-shell, the validity of the IMME were tested for the first time after the mass measurements of $^{41}$Ti, $^{45}$Cr, $^{49}$Fe and $^{53}$Ni with the IMS at the CSRe. The results are plotted in Fig. 17. It can be seen that for all quartets except for $A = 53$ the corresponding $d$-coefficients are comparable with zero. And neither the existing nor the new theoretical calculations of isospin mixing can explained this disagreement [50]. Subsequent

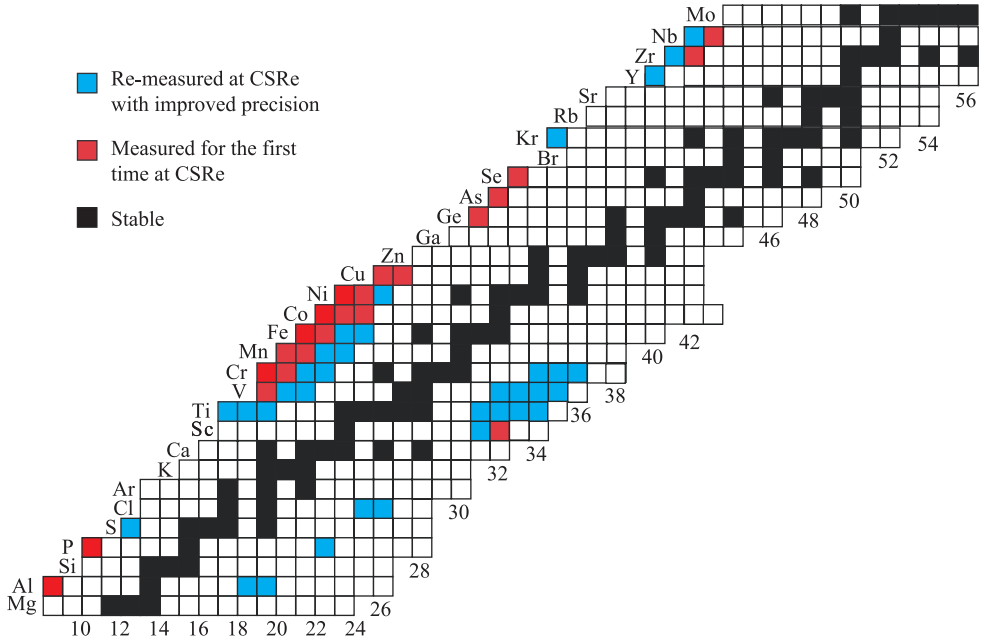


**Fig. 16** The partial chart of nuclides. Stable nuclides are shown with black colour. The nuclei whose masses were measured for the first time are indicted with red colour. The blue colour represents the remeasured nuclei with improved precision.

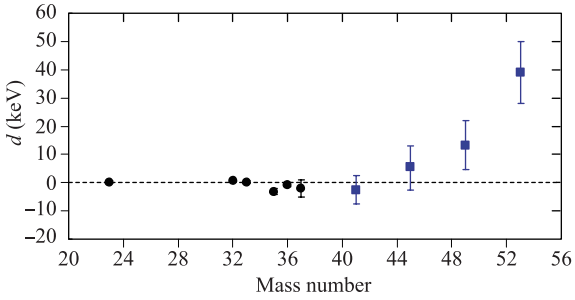


**Fig. 17** $d$ coefficients for the four $T = 3/2$ isobaric multiplets in $pf$-shell (squares). Experimental data since 2001 (circles) [83–86] are shown for comparison. Note, that albeit the large uncertainties, there seems to be a trend of gradual increase of d with $A$ in fp-shell. Reproduced from Ref. [50].

measurement of the $\beta$-delayed $\gamma$ deexcitation of $^{53}$Ni confirmed a new assignment of IAS in $^{53}$Co lower than the previous one [87]. And based on the new mass of $^{53}$Co$^{IAS}$, the quadratic form of IMME holds well for $A = 53$ quartet. Meanwhile similar situation happens to the case of $^{52}$Co. The $T = 2$, $J^{\pi} = 0^{+}$ IAS in $^{52}$Co was proposed in Ref. [88, 89] based on the data from the $\beta$-delayed proton decay of $^{52}$Ni. However an extreme large non-zero $d$ coefficient is obtained from the cubic IMME, and the c coefficient dramatically deviates from a smooth trend [80]. To exclude the possible reason of erroneous assignment, the energy level of IAS should be established using $\beta$-delayed $\gamma$ deexcitation of $^{52}$Ni. The predominant $\gamma$ rays of $\beta-\gamma$ of $^{52}$Ni originate from a cascade decay of the expected IAS in $^{52}$Co [88, 89], and the more probable decay mode of the first excited state of low-lying isomer $2^{+}$ in $^{52}$Co is $\beta$ decay [90], the masses of $^{52g}$Co and $^{52m}$Co are necessary to make a firm assignment of IAS in $^{52}$Co.

To understand the decay properties of $^{52}$Ni, the masses of $^{52g}$Co and $^{52m}$Co were measured with high precision through the IMS experiments at CSRe [53]. $ME(^{52g}Co) = -34361(8)$ keV and $ME(^{52m}Co) = -33974(10)$ keV are obtained respectively. These yield $E_x = 387(17)$ keV of excitation energy for the low-lying isomer $2^{+}$.

Since the masses of $^{52g,52m}$Co have been measured, the $ME(^{52}\mathrm{Co}^{IAS}) = -31426(10)$ keV was independently determined by the deexited $\gamma$ rays from the IAS to the $(2^{+})$ isomer [88, 89]. It calls for an interpretation that the observed $\beta$-delayed $\gamma$ and proton in the decay of $^{52}$Ni are from two different excited states in $^{52}$Co. And the predominant proton emissions are assigned to the decays of $1^{+}$ states which are lower than the $T = 2$, $J^{\pi} = 0^{+}$ IAS. Based on this work, the partial decay scheme of $^{52}$Ni are reconstructed, see Fig. 18.

By using the new mass of $^{52}$Co$^{IAS}$, the mass excesses of the four members of the $A = 52$, $T = 2$ isobaric multiplet are found to be consistent with the quadratic form of the IMME, which supports the assignment of IAS in this work. The newly determined level scheme of $^{52}$Co is consistent with its mirror nucleus $^{52}$Mn and can well be reproduced by large-scale shell model calculations using an isospin nonconserving Hamiltonian (see Fig. 18). Our theoretical calculations also indicate that the isospin mixing in the $T = 2$, $J^{\pi} = 0^{+}$ state in $^{52}$Co is extremely low, thus leading to a negligibly small proton emission from this state [53].

### 4.2 The masses of $^{29}$S and isospin non-conserving force in *sd* shell

As has been discussed in Ref. [91], the $b$ and $c$ coefficients of IMME are related to the isovector and isotensor components of the isospin non-conserving interactions.

Removing the known gross $A$ dependence of the $b$ and $c$ coefficients, a more detailed picture is exhibited by plotting the so-called Coulomb radius parameters defined as [92]

$$r_{0b} = \frac{3}{5}\frac{e^2(1-A)}{(b-\Delta_{nH})A^{1/3}}, \quad r_{0c} = \frac{3}{5}\frac{e^2}{cA^{1/3}}, \tag{11}$$

where $\Delta_{nH} = 782.3$ keV is the hydrogen-neutron mass difference. The ratio of the $r_{0b}$ and $r_{0c}$ radii, $R$, is defined as [92]

$$R = \frac{b-\Delta_{nH}}{c(1-A)}, \tag{12}$$

where the ratio, $R$, as a function of $A$ can be obtained through the $b$ and $c$ coefficients.

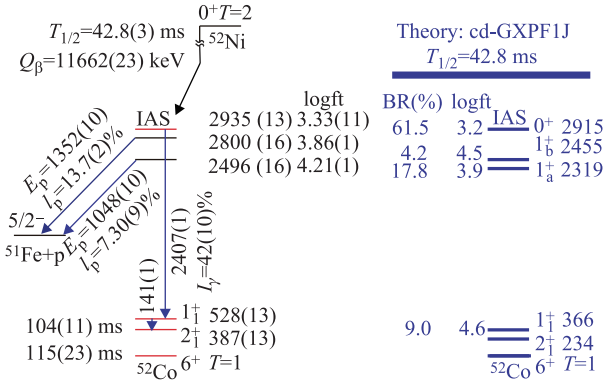


**Fig. 18** Partial decay scheme of $^{52}$Ni (left) and theoretical level structure of $^{52}$Co (right). Excitation energies are in keV. The theoretical branching ratios (BRs) and log $ft$ values based on cd-BGXPF1J are deduced from the present $Q$ value. The red levels are deduced from the ground-state mass of $^{52}$Co and the $\gamma$-ray energies from Ref. [89]. The black levels are determined from the $\beta-p$ data. Reproduced from Ref. [53].

According to Eqs. (11) and (12) using the $b$ and $c$ coefficients from cubic fits, the radius parameters $r_{0b}$ and $r_{0c}$, and the $R$ values are calculated. Previous investigations have shown that experimentally deduced $R$ values fluctuated around the unity, $R = 1$, indicating there was no obvious difference between $r_{0b}$ and $r_{0c}$ [92]. The reason is mainly due to large mass uncertainties in the early stage. Based on the newest data compiled in Ref. [80] and the most recent mass measurements [81, 82], the deduced results are shown in Fig. 19. It can be seen from Fig. 19 that $r_{0c}$ are definitely lower than $r_{0b}$, and all $R$ values fall to a constant value of about 0.96 with only exception of the $A = 9$ multiplet.

CSRe experiments yielded a more precise mass exess $ME(^{29}\mathrm{S}) = -3094(13)$ keV and a remeasured mass excess $ME(^{27}\mathrm{P}) = -685(42)$ keV [55]. The deduced $b$ and $c$ coefficients using the new masses also confirm that the constant $R$ value is around 0.96 (see Fig. 19).

We note that $R = 1$ holds under the assumptions that the nucleus is a uniformly charged sphere with the Coulomb radius $R_c = r_0\ A^{1/3}$ and the Coulomb interaction is the only source of the isospin-symmetry breaking. The deviation of $R$ from unity reflects the incompleteness of these assumptions and suggests the inevitable role of nuclear interaction in breaking the isospin symmetry. Meanwhile the confirmation of the constant $R$ value can be used to set experimental constraint for theoretical shell model calculations with isospin nonconserving forces [55].

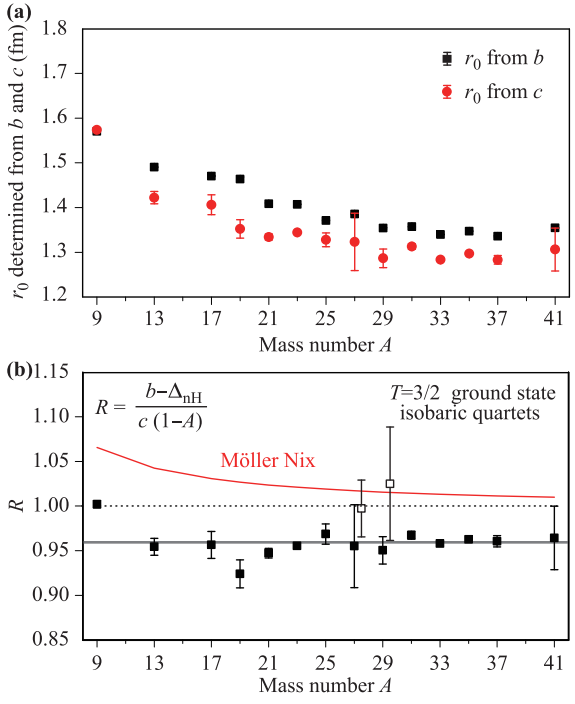


**Fig. 19** Top: Coulomb radius parameters determined from the $b$ and $c$ coefficients of the cubic IMME vs. mass number $A$. Bottom: The quantity $R$ plotted vs. $A$ for $T = 3/2$ isobaric quartets. The previously known $R$-values for $A = 27$ and 29 are shown with open symbols. For a uniform sphere $R = 1$. The red solid line is derived using the expressions in Ref. [93] for the liquid-droplet model [94]. The black line at $R = 0.96$ is to guide the eye. Reproduced from Ref. [55].

### 4.3 Persistence of neutron magic number $N = 32$ in Sc isotopes

More than 60 years ago, Mayer and Jense introduced nuclear shell model [95]. Since then, experimental evidence for magic number proved the existence of shell in nuclei around $\beta$-stability line and single particle level was also suggested [96]. In recent years new magic numbers appear in exotic nuclei toward the drip lines, and become a frontier of nuclear physics research [24–26, 97]. For specified neutron-rich nuclei, the appearance of the new magic number $N = 16$ and collapse of the traditional magic number $N = 28$ were confirmed [25, 98]. In $fp$-shell, the magic number $N = 32$ has been found in Ca [99], Ti [100], and Cr [101] isotopes by investigating the experimental systematic behavior of the $E(2^+)$ energies as a function of neutron number. Furthermore magic number $N = 32$ in Ca isotopes was also confirmed by precise mass measurements of $^{51,52}$Ca and $^{53,54}$Ca with Penning trap and multi reflection time-of-flight mass spectrometer of ISOTRAP at CERN respectively [97] through the two-neutron separation energy defined as

$$S_{2n} = ME(Z, N-2) - ME(Z, N) + 2ME(n), \quad (13)$$

where $ME(Z, N)$ is the mass excess of the nuclide with $Z$ protons and $N$ neutrons. The measured results show an excellent agreement with the prediction of microscopic calculations with three-nucleon forces ($NN + 3N$) using many-body perturbation theory for the valence-neutron interactions [97, 102]. However, it is worth noting that all of these are found in even-$Z$ nuclei.

Measurements of neutron-rich $^{86}$Kr projectile fragments at CSRe provided masses for odd-$Z$ nuclei $^{52}$Sc, $^{53}$Sc and $^{54}$Sc [27]. By using these masses and others in AME′12 [103], $S_{2n}$ as a function of neutron number is given to $N = 34$, and the shell closure can be observed until to $N = 32$ in the Sc isotopic chain.

The obtained $S_{2n}$ values are plotted in Fig. 20 together with results for the Ca and K isotopic chains. It can be seen that a reduction of $S_{2n}$ appears at $N = 32$ in both Sc and Ca isotopic chains and is as steep as the decrease at $N = 28$. Although the magic number of $N = 32$ has been introduced in many experiments, it was found in odd-$Z$ nuclei for the first time [27]. The theoretical calculation is in process, and the change of single particle level is highly expected, which is similar to neutron-rich Ca isotopes [24].

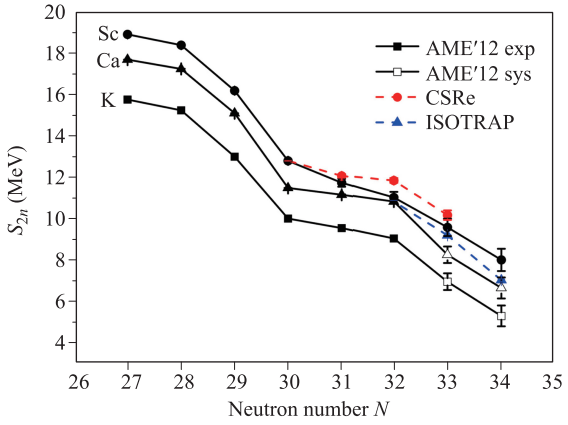


**Fig. 20** Two-neutron separation energy $S_{2n}$ as a function of neutron number $N$ for the K (squares), Ca (triangles), and Sc (circles) isotopic chains. Solid symbols represent values based on experimental data, hollow ones are estimated in AME′12 [103]. The red and blue ones are derived from mass values in this work and ISOTRAP [97], respectively. Reproduced from Ref. [27].

### 4.4 The masses of neutron-deficient Y, Zr, and Nb isotopes and the Zr-Nb cycle in the *rp*-process

Previously the $^{64}$Ge waiting point and Ca-Sc cycle in the *rp*-process were investigated by the measured masses of $^{65}$As and $^{45}$Cr at CSRe, respectively [51, 74]. It was found that $^{64}$Ge is not a significant *rp*-process waiting point nuclide and that the formation of the predicted Ca-Sc cycle in X-ray bursts can be excluded.

Recent CSRe experiments yielded the masses of $^{82}$Zr, $^{84}$Nb for the first time and more precise masses of $^{79}$Y, $^{81}$Zr and $^{83}$Nb [54]. The masses of $^{80}$Zr and $^{84}$Mo were also obtained using the systematics of nuclear separation energy. This resulted in an enhanced $\alpha$ separation energies ($S_\alpha$) at $^{84,85,86}$Mo as shown in Fig. 21. It can be seen that the claimed pronounced low-$S_\alpha$S island predicted by FRDM′92 [104] in neutron-deficient Mo isotopes does not exist, if our accurate masses of $^{81,82}$Zr and extrapolated masses of $^{80}$Zr, $^{84}$Mo are used.

The predicted Zr-Nb cycle in the *rp*-process of type I X-ray bursts is characterized by large $^{84}$Mo$(\gamma,\alpha)^{80}$Zr and $^{83}$Nb$(p,\alpha)^{80}$Zr reaction rates, which sensitively depend on $S_\alpha(^{84}\mathrm{Mo})$ [105]. The non-existence of the low-$S_\alpha$ island indicates that the expected large $^{84}$Mo$(\gamma,\alpha)^{80}$Zr and $^{83}$Nb$(p,\alpha)^{80}$Zr reaction rates could significantly be reduced, leading to a weakening or even disappearance of the Zr-Nb cycle.

Here we assume the $1\sigma$ upper or lower limits of mass uncertainties which give the largest $Q$-value for the $^{83}$Nb$(p,\alpha)^{80}$Zr reaction and the smallest $\alpha$ separation energy of $^{84}$Mo [106]. If our new results are used, the reaction rates favoring the formation of the Zr-Nb cycle are reduced by orders of magnitude. Fig. 22 shows the cycle branching ratio as a function of burst time for a typical burst under the favorable conditions [107]. It concludes, if our new masses are taken, that the favorable branching ratio into the Zr-Nb cycle is decreased, as demonstrated by the red line in Fig. 22, by several orders of magnitude even at the peak temperature of ∼1.9 GK. Until recently it has been assumed that at high temperatures (above 2 GK) the *rp*-process flow stalls at the $^{56}$Ni waiting point. The recent mass measurement of $^{56}$Cu questioned the

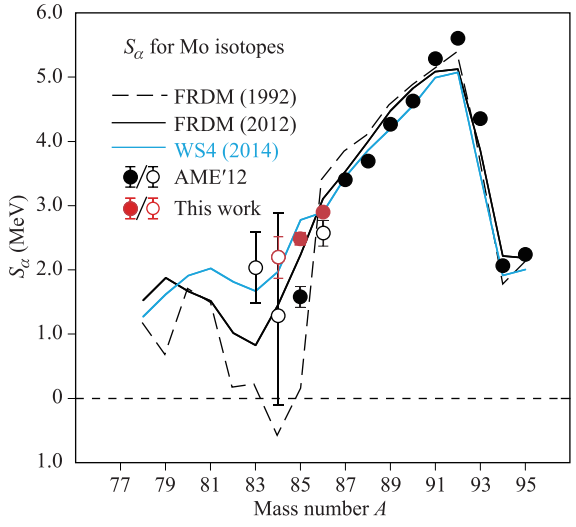


**Fig. 21** $\alpha$ separation energies, $S_\alpha$, for Mo isotopes. The open circle indicates $S_\alpha$ from at least one extrapolated mass value. The lines are from different mass models (see text). Reproduced from Ref. [54].

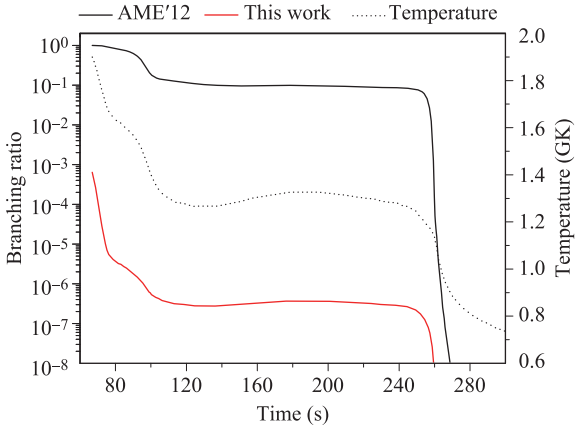


**Fig. 22** Fraction of the reaction flow branching into the Zr-Nb cycle under the most favorable conditions (see text for details) if using the masses from AME′12 (black line) and from this work (red line). The dashed black line shows the temperature varying within the burst time. For clarity, only the cooling stage is presented. Reproduced from Ref. [54].

stall of *rp*-process flow at the $^{56}$Ni waiting point [108]. There might be a possibility of an rp-process environment beyond $^{56}$Ni or with slowly rising temperature to make the flow pass through $^{56}$Ni before reaching high temperatures. In such cases, the Zr–Nb cycle may have been relevant as a further hindrance until temperatures declined down to 1.7 GK. Our new results with certainty remove this barrier [54].

### 4.5 Fundamental tests of the properties of the electroweak interaction

For any superallowed $0^+ \to 0^+$ $\beta$-decay between $T = 1$ analog states, $ft$ value can probe the conserved vector current (CVC) hypothesis, set limits on the presence of scalar currents, and provide the most precise value for $V_{ud}$, the up-down quark-mixing element of the Cabibbo–Kobayashi–Maskawa (CKM) matrix (see Refs. [109, 110]). The CVC hypothesis asserts that the weak vector coupling constant, $G_V$, is not renormalized in the nuclear medium. As experimental $ft$ value can be related to the $G_V$, a corrected $\mathcal{F}t$ with small corrections can be given by

$$\begin{aligned}\mathcal{F}t &\equiv ft(1+\delta'_R)(1+\delta_{NS}-\delta_C)\\ &= \frac{K}{2G_V^2(1+\Delta_R^V)},\end{aligned} \tag{14}$$

where $K/(\hbar c)^6 = 2\pi^3\hbar\ln 2/(m_e c^2)^5 = 8120.2787(11) \times 10^{-10}$ GeV$^{-4}$·s, $\delta_C$ is the isospin-symmetry-breaking correction, $\delta'_R$ and $\delta_{NS}$ are transition-dependent parts of radiative correction, and $\Delta_R^V$ is the transition-independent part. The $Q_{EC}$ value is required to determine the statistical rate function, $f$, while the half-life and branching ratio are combined to yield the partial half-life, $t$. As $f$ is approximately proportional to the fifth power of $Q_{EC}$ value, it is essential to determine the $Q_{EC}$ with the highest possible precision. According to Eq. (14), each measured transition can establish an individual value for $G_V$. If CVC hypothesis is confirmed, all the $\mathcal{F}t$ values should be identical within uncertainties regardless of nuclear species. $V_{ud}$ matrix element also can be extracted from $G_V$ to test the unitarity of the CKM matrix, a fundamental property of the electroweak Standard Model [109].

There are 20 $0^+ \to 0^+$ $\beta$ decays that have been surveyed recently [110]. After this the branching ratios and half-lifes of $^{42}$Ti, $^{46}$Cr, $^{50}$Fe and $^{54}$Ni are reported [111], a similar survey was performed soon and the number of such transition is increased to 23 [112]. However, the measurements for the four nuclei were not precise enough to test the CVC hypothesis stringently, thus, high-precision measurements are highly needed.

To improve the precision of these $ft$ values, the masses of $^{46}$Cr, $^{50}$Fe and $^{54}$Ni were measured with higher precision at CSRe [42]. The masses of $^{50}$Fe and $^{54}$Ni have precision improved by a factor of more than 10, and the uncertainties of the corresponding $\mathcal{F}t$ values are reduced by half consequently. The results are depicted in Fig. 23. It can be seen that our new results are in a good agreement with the latest averaged value of $\mathcal{F}t = 3072.27(72)$ s [110]. However the uncertainties of $\mathcal{F}t$ values are still too large to test the CVC hypothesis stringently. Fig. 24 presents fractional uncertainties of the experimental and theoretical input factors contributing to the final $\mathcal{F}t$ values for the superallowed transitions of $^{46}$Cr, $^{50}$Fe and $^{54}$Ni. We note that the limiting factor is changed to the uncertainty of the branching ratio after that the masses of $^{46}$Cr, $^{50}$Fe and $^{54}$Ni were remeasured at CSRe.

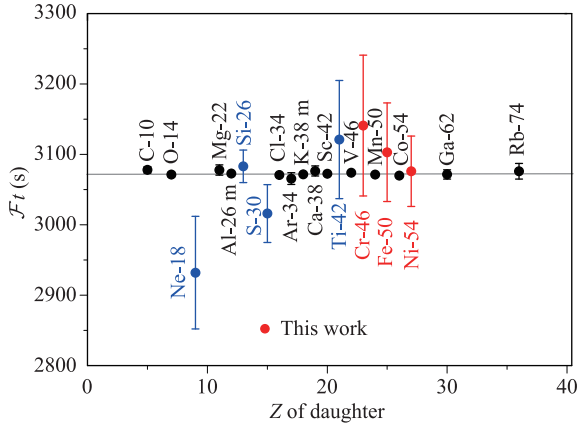


**Fig. 23** $\mathcal{F}t$ values plotted as a function of the charge of the daughter nucleus, $Z$. The black circles stand for the fourteen most precise values of the twenty cases surveyed in Ref. [110], the blue circles for the potential candidates compiled in Ref. [110], and the red ones from this work. The grey line at $\mathcal{F}t = 3072.27$ s is to guide the eye. Reproduced from Ref. [42].

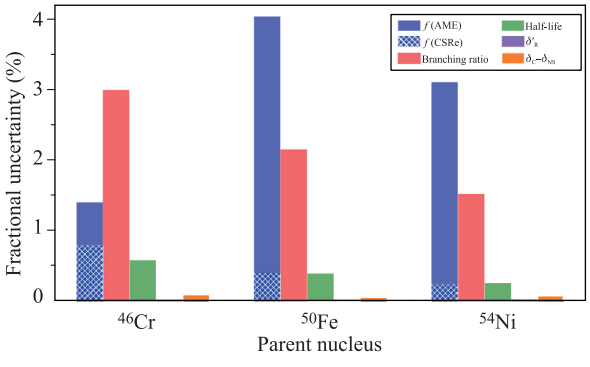


**Fig. 24** Fractional uncertainties of the experimental and theoretical input factors contributing to the final $\mathcal{F}t$ values of the superallowed transitions of $^{46}$Cr, $^{50}$Fe, and $^{54}$Ni. The data are from this work and Refs. [110, 112]. Reproduced from Ref. [42].

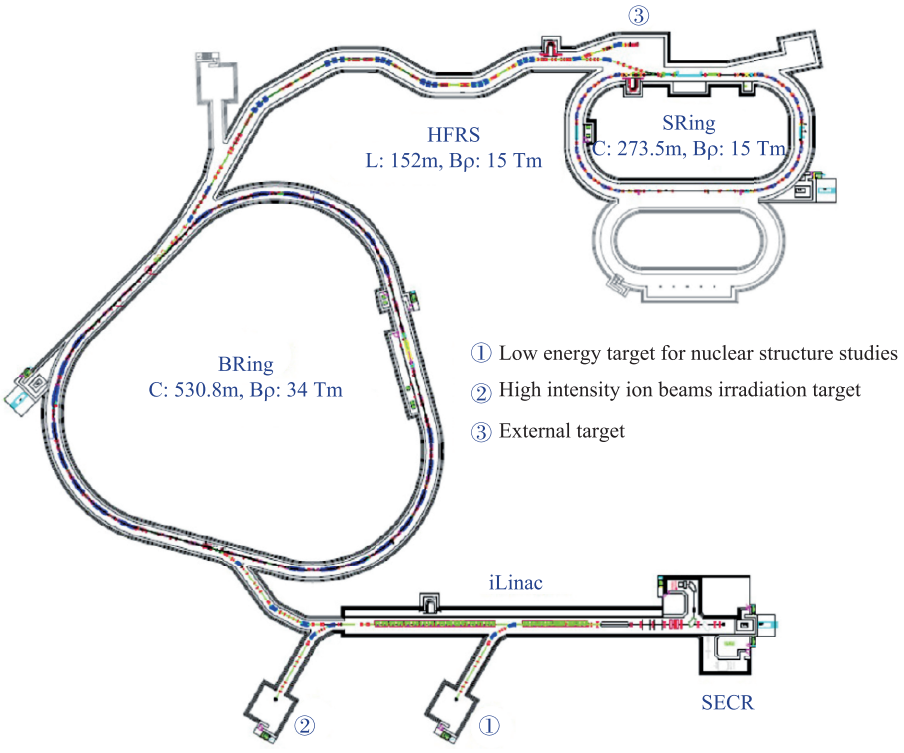


**Fig. 25** Current schematic layout of the HIAF facilities. Reproduced from Ref. [117].

## 5 Summary

In the last decade, the IMS conducted at HIRFL-CSR have been demonstrated as an excellent tool for direct mass measurements of short-lived nuclei. In this contribution, we presented recent results that have been successfully applied to the investigations of nuclear structure and nuclear astrophysics. In addition, technical developments in IMS experiments are also described.

## 6 Future perspectives

Although the present experimental program at the HIRFL-CSR facility has been successful and has contributed to several discoveries in physics investigations [37, 113], we still face severe limitations concerning the intensities of primary beams and the transmission efficiency of the CSRe for hot fragments. The next-generation storage ring facility HIAF (High Intensity heavy ion Accelerator Facility), which will be built in Huizhou, China, will solve these shortcomings [114]. The goal of HIAF project is to provide high-intensity, high-quality and high-energy beams for researches in nuclear structure of exotic nuclei, nucleosynthesis paths in the nuclear astrophysics, nuclear fusion mechanism, atomic physics and applied science [115]. Figure 25 shows the current schematic layout of the HIAF facility, which is composed of the Superconducting Electron-Cyclotron-Resonance ion source (SECR), the heavy ion Linac (iLinac) [116], the Booster Ring (BRing), the Fragment Separator (HFRS) with a large momentum acceptance $\Delta p/p = \pm 2.0 \times 10^{-2}$, the Spectrometer Ring (SRing) and several experimental setups [117]. As an essential part of the HIAF, the SRing is a dedicated storage ring for precision mass and half-life measurements of short-lived nuclei far from the valley of $\beta$-stability. The new facility shall offer new complementary research opportunities for storage ring physics as compared to the corresponding programs at GSI/FAIR storage ring [118–120], RARE RI-RING in RIKEN [121], and TSR@ISOLDE in CERN [122].

**Acknowledgements** This review paper is fully dedicated to celebrating Professor Akito Arima's 88th birthday. We express our sincere thanks to Prof. Akito Arima for promoting the collaboration between China and Japan in nuclear physics over the past decades, and particularly for his support on building the Cooler Storage Ring in Lanzhou, which is now a leading facility in the world for precision mass measurement of short-lived nuclei. This work was supported in part by the National Key R&D Program of China (Grant Nos. 2016YFA0400504 and 2018YFA0404400), the Key Research Program of Frontier Sciences of CAS (Grant No.

QYZDJ-SSW-S), and the Helmholtz-CAS Joint Research Group HCJRG-108.

## References


1. G. Audi, The history of nuclidic masses and of their evaluation, *Int. J. Mass Spectrom.* 251, 85 (2006)
2. K. Blaum, High-accuracy mass spectrometry with stored ions, *Phys. Rev.* 425, 1 (2006)
3. D. Lunney, J. M. Pearson, and C. Thibault, Recent trends in the determination of nuclear masses, *Rev. Mod. Phys.* 75, 1021 (2003)
4. A. S. Eddington, The internal constitution of the stars, *Nature* 106, 14 (1920)
5. F. W. Aston, A new mass spectrograph and the whole-number rule, *Proc. Roy. Soc. A* 115, 487 (1927)
6. F. W. Aston, Mass spectra and isotopes, *Nobel Lecture*, (1922)
7. G. Gamow, Mass defect curve and nuclear constitution, *Proc. Royal Society A* 126, 632 (1930)
8. C. F. von Weizsäcker, Zur Theorie der Kernmassen, *Z. Phys.* 96, 431 (1935)
9. H. A. Bethe und R. F. Bacher, Stationary states of nuclei, *Rev. Mod. Phys.* 8, 82 (1936)
10. A. J. Dempster, A new method of positive ray analysis, *Phys. Rev.* 11, 316 (1918)
11. J. H. E. Mattauch, W. Thiele, and A. H. Wapstra, 1964 Atomic mass table, *Nucl. Phys.* 67, 1 (1965)
12. H. Ewald and H. Hintenberger, Methoden und Anwendungen der Massenspektroskopie, *Zeitschrift Naturforschung Teil A* 8, 338 (1953)
13. F. Everling, L. A. König, J. H. E. Mattauch, and A. H. Wapstra, Relative nuclidic masses, *Nucl. Phys.* 18, 529 (1960)
14. K. Blaum and Yu. A. Litvinov (Eds.), 100 Years of Mass Spectrometry, *Int. J. Mass Spectr.* 349–350, 1 (2013)
15. H. Geissel, et al. (Ed.), Encyclopedia of Nuclear Physics and its Applications, 1st Ed., Wiley-VCH, Weinheim, 2013
16. T. Kubo, In-flight RI beam separator BigRIPS at RIKEN and elsewhere in Japan, *Nucl. Instrum. Methods Phys. Res. B* 204, 97 (2003)
17. J. Kurcewicz, F. Farinon, H. Geissel, S. Pietri, C. Nociforo, et al., Discovery and cross-section measurement of neutron-rich isotopes in the element range from neodymium to platinum with the FRS, *Phys. Lett. B* 717, 371 (2012)
18. J. Erler, N. Birge, M. Kortelainen, W. Nazarewicz, E. Olsen, A. M. Perhac, and M. Stoitsov, The limits of the nuclear landscape, *Nature(London)* 486, 509 (2012)
19. X. W. Xia, Y. Lim, P. W. Zhao, H. Z. Liang, X. Y. Qu, Y. Chen, H. Liu, L. F. Zhang, S. Q. Zhang, Y. Kim, and J. Meng, The limits of the nuclear landscape explored by the relativistic continuum Hartree–Bogoliubov theory, *Atomic Data and Nuclear Data Tables* 121–122, 1 (2018)
20. M. Wang, G. Audi, F. G. Kondev, W. J. Huang, S. Naimi, and X. Xu, The AME2016 atomic mass evaluation (II): Tables, graphs and references, *Chin. Phys. C* 41, 030003 (2017)
21. J. Dobaczewski, I. Hamamoto, W. Nazarewicz, and J. A. Sheikh, Nuclear shell structure at particle drip lines, *Phys. Rev. Lett.* 72, 981 (1994)
22. T. Otsuka, R. Fujimoto, Y. Utsuno, B. A. Brown, M. Honma, and T. Mizusaki, Magic numbers in exotic nuclei and spin-isospin properties of the $NN$ Interaction, *Phys. Rev. Lett.* 87, 082502 (2001)
23. L. Satpathy and S. K. Patra, New magic numbers and new islands of stability in drip-line regions in mass model, *Nucl. Phys. A* 722, C24 (2003)
24. D. Steppenbeck, S. Takeuchi, N. Aoi, P. Doornenbal, M. Matsushita, et al., Evidence for a new nuclear "magic number" from the level structure of $^{54}$Ca, *Nature* 502, 207 (2013)
25. A. Ozawa, T. Kobayashi, T. Suzuki, K. Yoshida, and I. Tanihata, New magic number, $N = 16$, near the neutron drip line, *Phys. Rev. Lett.* 84, 5493 (2000)
26. R. Kanungo, A new view of nuclear shells, *Phys. Scr.* T152, 014002 (2013)
27. X. Xu, M. Wang, Y.-H. Zhang, H.-S. Xu, P. Shuai, et al., Direct mass measurements of neutron-rich $^{86}$Kr projectile fragments and the persistence of neutron magic number $N = 32$ in Sc isotopes, *Chin. Phys. C* 39, 106201 (2015)
28. E. M. Burbidge, G. R. Burbidge, W. A. Fowler, and F. Hoyle, Synthesis of the elements in stars, *Rev. Mod. Phys.* 29, 547 (1957)
29. H. Schatz, Nuclear masses in astrophysics, *International Journal of Mass Spectrometry* 349–350, 181 (2013)
30. D. Martin, A. Arcones, W. Nazarewicz, and E. Olsen, Impact of nuclear mass uncertainties on the $\gamma$ process, *Phys. Rev. Lett.* 116, 121101 (2016)
31. R. Knöbel, M. Diwisch, H. Geissel, Yu. A. Litvinov, Z. Patyk, et al., New results from isochronous mass measurements of neutron-rich uranium fission fragments with the FRS-ESR-facility at GSI, *Eur. Phys. J. A* 52, 138 (2016)
32. K. Blaum, M. Block, R. B. Cakirli, S. Eliseev, M. Kowalska, S. Kreim, Y. A. Litvinov, Sz. Nagy, W. Nortershauser, and D. T. Yordanov, Measurements of ground-state properties for nuclear structure studies by precision mass and laser spectroscopy, *J. Phys. Conf. Ser.* 312, 092001 (2011)
33. K. Blaum, J. Dilling, and W. Nortershauser, Precision atomic physics techniques for nuclear physics with radioactive beams, *Phys. Scr. T*152, 014017 (2013)

34. B. Franzke, H. Geissel, and G. Münzenberg, Mass and lifetime measurements of exotic nuclei in storage rings, *Mass Spec. Rev.* 27, 428 (2008)
35. P. Egelhof, Y. Litvinov and M. Steck, Proceedings of the 9th International Conference on Nuclear Physics at Storage Rings STORI'14, *Phys. Scr.* 2015, 010301 (2015)
36. H. Geissel, Yu. A. Litvinov, F. Attallah, K. Beckert, P. Beller, et al., New results with stored exotic nuclei at relativistic energies, *Nucl. Phys. A* 746, 150c (2004)
37. Y. H. Zhang, Y. A. Litvinov, T. Uesaka and H. S. Xu, Storage ring mass spectrometry for nuclear structure and astrophysics research, *Phys. Scr.* 91, 073002 (2016)
38. X. Gao, Y. J. Yuan, J. C. Yang, S. Litvinov, M. Wang, Y. Litvinov, W. Zhang, D. Y. Yin, G. D. Shen, W. P. Chai, J. Shi, and P. Shang, Isochronicity corrections for isochronous mass measurements at the HIRFL-CSRe, *Nucl. Instr. Meth. in Phys. Res. Sect. A* 763, 53 (2014)
39. J. W. Xia, W. L. Zhan, B. W. Wei, Y. J. Yuan, M. T. Song, et al., The heavy ion cooler-storage-ring project (HIRFL-CSR) at Lanzhou, *Nucl. Instr. Meth. in Phys. Res. Sect. A* 488, 11 (2002)
40. Y. J. Yuan, J. C. Yang, J. W. Xia, P. Yuan, W. M. Qiao, et al., Status of the HIRFL–CSR complex, *Nucl. Instrum. Methods Phys. Res. B* 317, 214 (2013)
41. B. Mei, X. L. Tu, M. Wang, H. S. Xu, R. S. Mao, et al., A high performance time-of-flight detector applied to isochronous mass measurement at CSRe, *Nucl. Instrum. Meth. A* 624, 109 (2010)
42. P. Zhang, X. Xu, P. Shuai, R. J. Chen, X. L. Yan, et al., High-precision $Q_{EC}$ values of superallowed $0^+ \to 0^+$ $\beta$-emitters $^{46}$Cr, $^{50}$Fe and $^{54}$Ni, *Phys. Lett. B* 767, 20 (2017)
43. M. Hausmann, J. Stadlmann, F. Attallah, K. Beckert, P. Beller, et al., Isochronous mass measurements of hot exotic nuclei, *Hyperfine Interactions* 132, 291 (2001)
44. X. L. Tu, M. Wang, Yu. A. Litvinov, Y. H. Zhang, H. S. Xu, et al., Precision isochronous mass measurements at the storage ring CSRe in Lanzhou, *Nucl. Instrum. Methods Phys. Res. A* 654, 213 (2011)
45. B. -H. Sun, H. Geissel, M. Hausmann, C. Kozhuharov, R. Knöbel, Yu. A. Litvinov, J. Meng, Z. Patyk, T. Radon, and C. Scheidenberger, Identification of time-of-flight spectra for isochronous mass measurements, *Chin. Phys. C* 33, 161 (2009)
46. Yu. A. Litvinov, H. Geissel, T. Radon, F. Attallah, G. Audi, et al., Mass measurement of cooled neutron-deficient bismuth projectile fragments with time-resolved Schottky mass spectrometry at the FRS-ESR facility, *Nucl. Phys. A* 756 3 (2005)
47. B. Sun, R. Knöbel, Yu. A. Litvinov, H. Geissel, J. Meng, et al., Nuclear structure studies of short-lived neutron-rich nuclei with the novel large-scale isochronous mass spectrometry at the FRS-ESR facility, *Nucl. Phys. A* 812 1 (2008)
48. A. Kankainen, V.-V. Elomaa, T. Eronen, D. Gorelov, J. Hakala, et al., Mass measurements in the vicinity of the doubly magic waiting point $^{56}$Ni, *Phys. Rev. C* 82 034311 (2010)
49. X. L. Tu, Mass measurements of short-lived $A = 2Z - 1$ nuclides at HIRFL-CSR, *Ph D Thesis, University of Chinese Academy of Sciences*, 2011
50. Y. H. Zhang, H. S. Xu, Yu. A. Litvinov, X. L. Tu, X. L. Yan, et al., Mass measurements of the neutron-deficient $^{41}$Ti, $^{45}$Cr, $^{49}$Fe, and $^{53}$Ni nuclides: First test of the isobaric multiplet mass equation in $fp$-Shell nuclei, *Phys. Rev. Lett.* 107, 102501 (2012)
51. X. L. Yan, H. S. Xu, Yu. A. Litvinov, Y. H. Zhang, H. Schatz, et al., Mass measurement of $^{45}$Cr and its impact on the Ca-Sc cycle in $X$-ray bursts, *Astrophys. J. Letters* 766, L8 (2013)
52. P. Shuai, H. S. Xu, Y. H. Zhang, Yu. A. Litvinov, M. Wang, et al., Accurate correction of magnetic field instabilities for high-resolution isochronous mass measurements in storage rings, arXiv: 1407.3459 [nucl-ex]
53. X. Xu, P. Zhang, P. Shuai, R. J. Chen, X. L. Yan, et al., Identification of the lowest $T = 2$, $J^\pi = 0^+$ isobaric analog state in $^{52}$Co and its impact on the understanding of $\beta$-decay properties of $^{52}$Ni, *Phys. Rev. Lett.* 117, 182503 (2016)
54. Y. M. Xing, K. A. Li, Y. H. Zhang, X. H. Zhou, M. Wang, et al., Mass measurements of neutron-deficient Y, Zr, and Nb isotopes and their impact on $rp$ and $\nu p$ nucleosynthesis processes, *Phys. Lett. B* 781, 358 (2018)
55. C. Y. Fu, Y. H. Zhang, X. H. Zhou, M. Wang, Yu. A. Litvinov, et al., Masses of the $T_z = -3/2$ nuclei $^{27}$P and $^{29}$S, *Phys. Rev. C* 98, 014315 (2018)
56. R. J. Chen, X. L. Yan, W. W. Ge, Y. J. Yuan, M. Wang, et al., A method to measure the transition energy $\gamma_t$ of the isochronously tuned storage ring, *Nucl. Instrum. Meth. A* 898, 111 (2018)
57. X. Xu, M. Wang, P. Shuai, R. J. Chen, X. L. Yan, et al., A data analysis method for isochronous mass spectrometry usingtwo time-of-flight detectors at CSRe, *Chin. Phys. C* 39, 106201 (2015)
58. P. Shuai, X. Xu, Y. H. Zhang, H. S. Xu, Yu. A. Litvinov, et al., An improvement of isochronous mass spectrometry: Velocity measurements using two time-of-flight detectors, *Nucl. Instrum. Methods Phys. Res. B* 376, 311 (2016)
59. W. Zhang, X. L. Tu, M. Wang, Y. H. Zhang, H. S. Xu, et al., Time-of-flight detectors with improved timing performance for isochronous mass measurements at the CSRe, *Nucl. Instrum. Meth. A* 756, 1 (2014)
60. Y. M. Xing, M. Wang, Y. H. Zhang, P. Shuai, X. Xu, et al., First isochronous mass measurements with two time-of-flight detectors at CSRe, *Phys. Scr.* 2015, 014010 (2015)

61. W. R. Phillips, I. Ahmad, D. W. Banes, B. G. Glagola, W. Henning, W. Kutschera, K. E. Rehm, J. P. Schiffer, and T. F. Wang, Charge-state dependence of nuclear lifetimes, *Phys. Rev. Lett.* 62, 1025 (1989)
62. M. Jung, F. Bosch, K. Beckert, H. Eickhoff, H. Folger, et al., First observation of bound-state $\beta$-decay, *Phys. Rev. Lett.* 69, 2164 (1992)
63. F. Attallah, M. Aiche, J. F. Chemin, J. N. Scheurer, W. E. Meyerhof, J. P. Grandin, P. Aguer, G. Bogaert, J. Kiener, A. Lefebvre, J. P. Thibaud, and C. Grunberg, Charge state blocking of K-shell internal conversion in $^{125}$Te, *Phys. Rev. Lett.* 75, 1715 (1995)
64. H. Irnich, H. Geissel, F. Nolden, K. Beckert, F. Bosch, et al., Half-life measurements of bare, mass-resolved isomers in a storage-cooler ring, *Phys. Rev. Lett.* 75, 4182 (1995)
65. F. Bosch, T. Faestermann, J. Friese, F. Heine, P. Kienle, et al., Observation of bound-state $\beta$-decay of fully ionized $^{187}$Re: $^{187}$Re-$^{187}$Os cosmochronometry, *Phys. Rev. Lett.* 77, 5190 (1996)
66. T. Ohtsubo, F. Bosch, H. Geissel, L. Maier, C. Scheidenberger, et al., Simultaneous measurement of $\beta$-decay to bound and continuum electron states, *Phys. Rev. Lett.* 95, 052501 (2005)
67. Yu. A. Litvinov, F. Bosch, H. Geissel, J. Kurcewicz, Z. Patyk, et al., Measurement of the $\beta^+$ and orbital electron-capture decay rates in fully ionized, hydrogen-like, and heliumlike $^{140}$Pr Ions, *Phys. Rev. Lett.* 99, 262501 (2007)
68. Yu. A. Litvinov, F. Bosch, N. Winckler, D. Boutin, H. G. Essel, et al., Observation of non-exponential orbital electron capture decays of hydrogen-like $^{140}$Pr and $^{142}$Pm ions, *Phys. Lett. B* 664, 162 (2008)
69. P. Kienle (for the Two-Body-Weak-Decays Collaboration), High-resolution measurement of the time-modulated orbital electron capture and of the $\beta^+$ decay of hydrogen-like $^{142}$Pm$^{60+}$ ions, *Phys. Lett. B* 726, 638 (2013)
70. J. N. Bahcall, Beta decay in stellar interiors, *Phys. Rev.* 126, 1143 (1962)
71. Q. Zeng, M. Wang, X. H. Zhou, Y. H. Zhang, X. L. Tu, et al., Half-life measurement of short-lived $^{94m}_{44}$Ru$^{44+}$ using isochronous mass spectrometry, *Phys. Rev. C* 96, 031303 (2017)
72. R. J. Chen, Y. J. Yuan, M. Wang, X. Xu, P. Shuai, et al., Simulations of the isochronous mass spectrometry at the HIRFL-CSR, *Phys. Scr.* 2015, 014044 (2015)
73. X. C. Chen, Q. Zeng, Yu. A. Litvinov, X. L. Tu, P. M. Walker, M. Wang, Q. Wang, K. Yue, and Y. H. Zhang, Statistical approaches to lifetime measurements with restricted observation times, *Phys. Rev. C* 96, 034302 (2017)
74. X. L. Tu, H. S. Xu, M. Wang, Y. H. Zhang, Yu. A. Litvinov, et al., Direct mass measurements of short-lived $A = 2Z - 1$ nuclides $^{63}$Ge, $^{65}$As, $^{67}$Se, and $^{71}$Kr and their impact on nucleosynthesis in the *rp* process, *Phys. Rev. Lett.* 106, 112501 (2011)
75. P. Shuai, H. S. Xu, X. L. Tu, Y. H. Zhang, B. H. Sun, et al., Charge and frequency resolved isochronous mass spectrometry and the mass of $^{51}$Co, *Phys. Lett. B* 735, 327 (2014)
76. E. P. Wigner, On the consequences of the symmetry of the nuclear hamiltonian on the spectroscopy of nuclei, *Phys. Rev.* 51, 106 (1937)
77. E. P. Wigner, in: Proc. of the R. A. Welch Foundation Conf. on Chemical Research, Houston, edited by W. O. Milligan (R. A. Welch Foundation, Houston, 1957), Vol. 1
78. S. Weinberg and S. B. Treiman, Electromagnetic Corrections to isotopic spin conservation, *Phys. Rev.* 116, 465 (1959)
79. M. B. Bennett, C. Wrede, B. A. Brown, S. N. Liddick, D. Pérez-Loureiro, et al., Isobaric multiplet mass equation in the $A = 31$, $T = 3/2$ quartets, *Phys. Rev. C* 93, 064310 (2016)
80. M. MacCormick and G. Audi, Evaluated experimental isobaric analogue states from $T = 1/2$ to $T = 3$ and associated IMME coefficients, *Nucl. Phys. A* 925, 61 (2014)
81. A. T. Gallant, M. Brodeur, C. Andreoiu, A. Bader, A. Chaudhuri, et al., Breakdown of the isobaric multiplet mass equation for the $A = 20$ and 21 multiplets, *Phys. Rev. Lett.* 113, 082501 (2014)
82. A. Kankainen, L. Canete, T. Eronen, J. Hakala, A. Jokinen, J. Koponen, I. D. Moore, D. Nesterenko, J. Reinikainen, S. Rinta-Antila, A. Voss, and J. Äystö, Mass of astrophysically relevant $^{31}$Cl and the breakdown of the isobaric multiplet mass equation, *Phys. Rev. C* 93, 041304(R) (2016)
83. R. Ringle, T. Sun, G. Bollen, D. Davies, M. Facina, J. Huikari, E. Kwan, D. J. Morrissey, A. Prinke, J. Savory, P. Schury, S. Schwarz, and C. S. Sumithrarachchi, High-precision Penning trap mass measurements of $^{37,38}$Ca and their contributions to conserved vector current and isobaric mass multiplet equation, *Phys. Rev. C* 75, 055503 (2007)
84. C. Yazidjian, G. Audi, D. Beck, K. Blaum, S. George, C. Guenaut, F. Herfurth, A. Herlert, A. Kellerbauer, H.-J. Kluge, D. Lunney, and L. Schweikhard, Evidence for a breakdown of the isobaric multiplet mass equation: A study of the $A = 35$, $T = 3/2$ isospin quartet, *Phys. Rev. C* 76, 024308 (2007)
85. A. Saastamoinen, T. Eronen, A. Jokinen, V.-V. Elomaa, J. Hakala, A. Kankainen, I. D. Moore, S. Rahaman, J. Rissanen, C. Weber, J. Äystö, and L. Trache, Mass of $^{23}$Al for testing the isobaric multiplet mass equation, *Phys. Rev. C* 80, 044330 (2009)
86. A. Kankainen, T. Eronen, D. Gorelov, J. Hakala, A. Jokinen, V. S. Kolhinen, M. Reponen, J. Rissanen, A. Saastamoinen, V. Sonnenschein, and J. Äystö, High-precision mass measurement of $^{31}$S with the double Penning trap JYFLTRAP improves the mass value for $^{32}$Cl, *Phys. Rev. C* 82, 052501(R) (2010)

87. J. Su, W. P. Liu, N. T. Zhang, Y. P. Shen, Y. H. Lam, et al., Revalidation of the isobaric multiplet mass equation at $A = 53$, $T = 3/2$, *Phys. Lett. B* 756, 323 (2016)

88. C. Dossat, N. Adimi, F. Aksouh, F. Becker, A. Bey, et al., The decay of proton-rich nuclei in the mass $A = 36$–$56$ region, *Nucl. Phys. A* 792, 18 (2007)

89. S. E. A. Orrigo, B. Rubio, Y. Fujita, W. Gelletly, J. Agramunt, et al., $\beta$ decay of the exotic $T_z = -2$ nuclei $^{48}$Fe, $^{52}$Ni, and $^{56}$Zn, *Phys. Rev. C* 93, 044336 (2016)

90. G. Audi, F. G. Kondev, M. Wang, W. J. Huang, and S. Naimi, The NUBASE2016 evaluation of nuclear properties, *Chin. Phys. C* 41, 030001 (2017)

91. M. A. Bentley and S. M. Lenzi, Coulomb energy differences between high-spin states in isobaric multiplets, *Prog. Part. Nucl. Phys.* 59, 497 (2007)

92. W. Benenson and E. Kashy, Isobaric quartets in nuclei, *Rev. Mod. Phys.* 51, 527 (1979)

93. Y. H. Lam, N. A. Smirnova, and E. Caurier, Isospin nonconservation in *sd*-shell nuclei, *Phys. Rev. C* 87, 054304 (2013)

94. P. Möller and J. R. Nix, Nuclear masses from a unified macroscopic-model, *At. Data Nucl. Data Tables* 39, 213 (1988)

95. M. Goeppert-Mayer, On closed shells in nuclei (II), *Phys. Rev.* 75, 1969 (1949)

96. I. Talmi, The shell model – Successes and limitations, *Nucl. Phys. A* 507, 295 (1990)

97. F. Wienholtz, D. Beck, K. Blaum, Ch. Borgmann, M. Breitenfeldt, et al., Masses of exotic calcium isotopes pin down nuclear forces, *Nature* 498, 346 (2013)

98. F. Sarazin, H. Savajols, W. Mittig, F. Nowacki, N. A. Orr, et al., Shape coexistence and the $N = 28$ shell closure far from stability, *Hyperfine Interactions* 132, 147 (2001)

99. A. Gade, R. V. F. Janssens, D. Bazin, R. Broda, B. A. Brown, et al., Cross-shell excitation in two-proton knockout: Structure of $^{52}$Ca, *Phys. Rev. C* 74, 021302 (2006)

100. R. V. F. Janssens, B. Fornal, P. F. Mantica, B. A. Brown, R. Broda, et al., Structure of $^{52,54}$Ti and shell closures in neutron-rich nuclei above $^{48}$Ca, *Phys. Lett. B* 546, 55 (2002)

101. J. I. Prisciandaro, P. F. Mantica, B. A. Brown, D. W. Anthony, M. W. Cooper, et al., New evidence for a subshell gap at $N = 32$, *Phys. Lett. B* 510, 17 (2001)

102. A. T. Gallant, J. C. Bale, T. Brunner, U. Chowdhury, S. Ettenauer, et al., New Precision Mass Measurements of Neutron-Rich Calcium and Potassium Isotopes and Three-Nucleon Forces, *Phys. Rev. Lett.* 109, 032506 (2012)

103. M. Wang, G. Audi, A. Wapstra, F. Kondev, M. MacCormick, X. Xu, and B. Pfeiffer, The AME2012 atomic mass evaluation (II): Tables, graphs and references, *Chin. Phys. C* 36, 1603 (2012)

104. P. Möller, J. Nix, W. D. Myers, and W. J. Swiatecki, Nuclear ground-state masses and deformations, *At. Data Nucl. Data Tables* 59, 185 (1995)

105. H. Schatz, A. Aprahamian, J. Görres, M. Wiescher, T. Rauscher, J. F. Rembges, F.-K. Thielemann, B. Pfeiffer, P. Möller, K.-L. Kratz, H. Herndl, B. A. Brown, and H. Rebel, *rp*-process nucleosynthesis at extreme temperature and density conditions, *Phys. Rep.* 294, 167 (1998)

106. E. Haettner, D. Ackermann, G. Audi, K. Blaum, M. Block, et al., Mass measurements of very neutron-deficient Mo and Tc isotopes and their impact on *rp* process nucleosynthesis, *Phys. Rev. Lett.* 106, 122501 (2011)

107. H. Schatz, A. Aprahamian, V. Barnard, L. Bildsten, A. Cumming, M. Ouellette, T. Rauscher, F.-K. Thielemann, and M. Wiescher, End Point of the *rp* Process on Accreting Neutron Stars, *Phys. Rev. Lett.* 86, 3471 (2001)

108. A. A. Valverde, M. Brodeur, G. Bollen, M. Eibach, K. Gulyuz, A. Hamaker, C. Izzo, W.-J. Ong, D. Puentes, M. Redshaw, R. Ringle, R. Sandler, S. Schwarz, C. S. Sumithrarachchi, J. Surbrook, A. C. C. Villari, and I. T. Yandow, High-precision mass measurement of $^{56}$Cu and the redirection of the *rp*-process flow, *Phys. Rev. Lett.* 120, 032701 (2018)

109. J. C. Hardy and I. S. Towner, New limits on fundamental weak-interaction parameters from superallowed $\beta$ decay, *Phys. Rev. Lett.* 94, 092502 (2005)

110. J. C. Hardy and I. S. Towner, Superallowed $0^+ \to 0^+$ nuclear $\beta$ decays: 2014 critical survey, with precise results for $V_{ud}$ and CKM unitarity, *Phys. Rev. C* 91, 025501 (2015)

111. F. Molina, B. Rubio, Y. Fujita, W. Gelletly, J. Agramunt, et al., $T_z = -1 \to 0$ $\beta$ decays of $^{54}$Ni, $^{50}$Fe, $^{46}$Cr, and $^{42}$Ti and comparison with mirror ($^3$He, t) measurements, *Phys. Rev. C* 91, 014301 (2015)

112. I. S. Towner and J. C. Hardy, Theoretical corrections and world data for the superallowed $ft$ values in the $\beta$ decays of $^{42}$Ti, $^{46}$Cr, $^{50}$Fe, and $^{54}$Ni, *Phys. Rev. C* 92, 055505 (2015)

113. M. Wang, H. S. Xu, Y. H. Zhang, X. L. Tu, Yu. A. Litvinov and CSRe collaboration, Mass measurement of short-lived nuclei at HIRFL-CSR, *EPJ Web of Conferences* 66, 02107 (2014)

114. J. C. Yang, J. W. Xia, G. Q. Xiao, H. S. Xu, H. W. Zhao, et al., High Intensity heavy ion Accelerator Facility (HIAF) in China, *Nucl. Instrum. Methods Phys. Res. B* 317, 263 (2013)

115. X. Ma, W. Q. Wen, S. F. Zhang, D. Y. Yu, R. Cheng, et al., HIAF: New opportunities for atomic physics with highly charged heavy ions, *Nucl. Instrum. Methods Phys. Res. B* 408, 169 (2017)

116. Z. J. Wang, Proceedings of LINAC2012, Tel-Aviv, Israel, TUPB039

117. B. Wu, J. C. Yang, J. W. Xia, X. L. Yan, X. J. Hu, et al., HIAF: New opportunities for atomic physics with highly charged heavy ions, *Nucl. Instrum. Methods Phys. Res. B* 408, 169 (2017)

118. Yu. A. Litvinov and F. Bosch, Beta decay of highly charged ions, *Rep. Prog. Phys.* 74, 016301 (2011)

119. T. Stöhlker, Yu. A. Litvinov, and A. Bräuning-Demian, M. Lestinsky, F. Herfurth, R. Maier, D. Prasuhn, R. Schuch, M. Steck, for the SPARC Collaboration, SPARC collaboration: New strategy for storage ring physics at FAIR, *Hyperfine Interact* 227, 45 (2014)

120. P. M. Walker, Yu. A. Litvinov, and H. Geissel, The ILIMA project at FAIR, *Int. J. Mass Spectr.* 349–350, 247 (2013)

121. T. Yamaguchia, Y. Yamaguchi, and A. Ozawa, The challenge of precision mass measurements of short-lived exotic nuclei: Development of a new storage ring mass spectrometry, *Int. J. Mass Spectr.* 349-350, 240 (2013)

122. M. Grieser, Yu. A. Litvinov, R. Raabe, K. Blaum, Y. Blumenfeld, et al., Storage ring at HIE-ISOLDE, *Eur. Phys. J.: Spec. Top.* 207, 1 (2012)